Design and Implementation of an Entanglement Harvesting Experiment With Superconducting Flux Qubits

by

Shaun Ren

A thesis
presented to the University of Waterloo
in fulfillment of the
thesis requirement for the degree of
Master of Science
in
Physics

Waterloo, Ontario, Canada, 2022

Author's Declaration

I hereby declare that I am the sole author of this thesis. This is a true copy of the thesis, including any required final revisions, as accepted by my examiners.

I understand that my thesis may be made electronically available to the public.

Abstract

Recent studies in relativistic quantum information have predicted that it is possible to entangle two qubits tunably coupled to the same quantum field in its vacuum state, by allowing the qubits to couple to the field for a very short amount of time, even if the coupling time forbids the formation of a lightlike connection between the qubits. This is made possible due to the correlations already present in the vacuum field. To date, no experiments have been performed to demonstrate this phenomenon.

Recent work by the superconducting quantum devices (SQD) group has produced a novel device, namely the superconducting flux qubit with a tunable ultrastrong coupler, has the properties especially suited for an entanglement harvesting experiment. The device, which allows light-matter interaction strength to be tuned from weak to ultrastrong coupling, opens the possibility of a realistic implementation of the experiment.

In this thesis, we propose a circuit quantum electrodynamics (QED) experiment using the newly designed device to detect the harvesting of entanglement from a one-dimensional quantum field. First, we derive the necessary theoretical model that allows us to analyze the feasibility of such an experiment. Then, we analyze the feasibility of the experiment and calculate the optimal parameters that allow the most entanglement to be harvested. Finally, using the optimal parameters, we propose a design for the experiment and validate the design through simulations.

Acknowledgements

I would like to express my deepest gratitude to my supervisor Prof. Adrian Lupaşcu, whose insight and knowledge into the subject matter guided me throughout this research. I am grateful for his exemplary dedication and discipline, and I am grateful for the opportunities provided to me.

Furthermore, I would like to thank Prof. Eduardo Martín-Martínez for the much appreciated discussions and guidance on the theoretical work, and for serving on my advisory and thesis committee. I am also thankful to Prof. Jan Kycia for serving on my advisory and thesis committee.

I would like to thank Jiahao Shi for designing the USC qubit with a tunable coupler. I am also grateful to Noah Cornelius Janzen for fabricating the device, and for setting up the electronics inside the dilution refrigerator. Their tireless efforts are essential towards the successful completion of this research.

I am also grateful to all the current and former members of the SQD group, including Jiahao Shi, Noah Cornelius Janzen, Michal Kononenko, Xi Dai, Dr. Muhammet Ali Yurtalan, Lucas Hak, Jae Jong Oh, Michael Tai, Denis Melanson, Dr. Salil Bedkihal, and Dr. Mehmet Canturk, for the many hours of insightful discussions, help, and support.

I am thankful to the Quantum NanoFab department, and the IQC IT department, for their assistance during my research.

Lastly, I would like thank my family and friends for their encouragement and support throughout my studies.

Table of Contents

List of Figures

List of Tables

Chapter 1

Introduction

1.1 Introduction

The harvesting of entanglement is a phenomenon where two quantum systems can become entangled without a lightlike connection forming between them [27, 28, 31], made possible by the preexisting correlations between spacelike-separated regions in a quantum field [32]. Aside from its importance in fundamental physics in quantum field theory, entanglement harvesting is also a key component in measuring the topology of spacetime [21], in quantum energy teleportation [14]. Moreover, entanglement harvesting has applications in quantum metrology such as quantum seismology [5]. Despite the tremendous importance of the phenomenon of entanglement harvesting, no experiment to date has been performed that can demonstrate this phenomenon.

Circuit QED is the field concerned with the study of light-matter interaction between artificial atoms such as superconducting qubits, and quantized electromagnetic fields [4]. Superconducting qubits are macroscopic nonlinear superconducting circuits that exhibit the same quantum behaviours as microscopic systems, such as a natural atom. Compared to natural atoms, superconducting qubits can be more easily manipulated and the coupling strength between a superconducting qubit and a quantum field can greatly exceed that of a natural atom.

A circuit QED experiment in 2017 [8] was able to demonstrate the ability for the coupling between the superconducting qubit and the quantum field to enter the so-called ultrastrong coupling (USC) regime, defined as the regime where the qubit's photon emission rate Γ_G is more than 10% of the qubit's transition frequency Δ. In the USC regime, the rotating-wave

approximation breaks down and novel phenomenologies emerge. Much phenomena has been predicted that can only be observed in this regime, including changes in the spectral features and intensity of the qubits [10], as well as changes in the physical properties of the qubits [9]. Due to the ability for artificial atoms to couple ultrastrongly to a quantum field, circuit QED is one of the most promising fields to study the dynamics of entanglement harvesting.

Recent work in the superconducting quantum devices (SQD) group, including [8] and [29], has led to a novel superconducting flux qubit with a tunable coupler that can couple to a one-dimensional quantum electromagnetic field from weak to ultrastrong coupling and beyond. This opens up the possibility of devising and performing an entanglement harvesting experiment based on this qubit. In this thesis, we analyze the feasibility of such an experiment and devise a device and a protocol that can be used to demonstrate the phenomenon of entanglement harvesting.

1.2 Outline of the Thesis

This thesis is organized as follows.

In chapter 2, we introduce the theoretical foundation required to analyze and design an entanglement harvesting experiment based on the novel USC qubit. This includes a discussion on the theory behind superconducting qubits, the control and readout of superconducting qubits, the quantization of a transmission line, and the Unruh-DeWitt model for light-matter interaction.

In chapter 3, we use perturbation theory to derive the expressions for the amount of entanglement observable under realistic experimental conditions, including finite temperature for the qubit and the transmission line. We find that non-negligible amounts of entanglement can be harvested from the quantum field with suitable device design parameters and initial qubit states.

In chapter 4, we present a device design and experimental protocol based on the calculations in chapter 3. Furthermore, we simulate our experiment and determine that it is realistic to generate enough entanglement between the qubits for detection using our proposed device and experimental protocol.

Chapter 2

Background

In this chapter, we introduce the background required for the design and implementation of an entanglement harvesting experiment with superconducting flux qubits. This chapter is organized as follows. In section 2.1, we introduce the theoretical foundation for a superconducting flux qubit, including the concepts required for the control and readout of such a qubit. In section 2.2, we introduce the circuit model of the transmission line and its quantization. Finally, in section 2.3, we introduce the Unruh-DeWitt detector model, which is used to model the dynamics of the entanglement harvesting experiment.

2.1 Superconducting Qubits

2.1.1 Josephson Junctions

The fundamental building block of superconducting qubits is the Josephson junction. The Josephson junction is formed by coupling two superconductors with a thin barrier, which is either an insulator, a non-superconducting piece of metal, or a physical constriction.

Brian David Josephson predicted in 1962 that in this configuration the macroscopic wave function of the two superconductors overlap at the insulating barrier, providing a means of tunneling without dissipation [17]. This mechanism is mediated by the tunneling of Cooper pairs across the barrier.

The energy stored in a Josephson junction depends on the phase difference $\gamma = \gamma_1 - \gamma_2$ between the wavefunctions of the superconductors [24], given by

$$U = -E_J \cos\gamma, \tag{2.1}$$

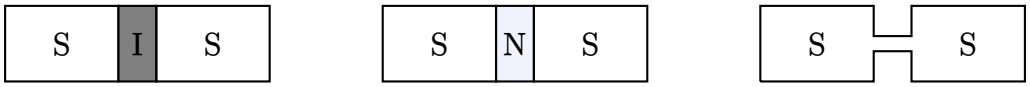

(a) SIS (b) SNS (c) ScS

Figure 2.1: Different types of Josephson junctions. (a) A superconductor-insulator-superconductor (SIS) junction, (b) A superconductor-metal-superconductor (SNS) junction, (c) a superconductor-constriction-superconductor (ScS) junction.

where

$$E_J = \varphi_0 I_C \tag{2.2}$$

is the Josephson energy, with $\varphi_0 = \Phi_0/2\pi$ being the reduced magnetic flux quantum, with the magnetic flux quntaum being defined as

$$\Phi_0 = \frac{h}{2e}, \tag{2.3}$$

and I_C the critical current of the junction. The critical current I_C is the maximum supercurrent that can flow across the junction. This critical current is related to the normal state resistance R_n, and the voltage gap V_g, of the junction, by the Ambegaokar-Baratoff relation [1]

$$I_C \approx \frac{V_\mathrm{g}}{R_\mathrm{n}}. \tag{2.4}$$

Josephson predicted the two equations that relate the current and voltage across the junction:

$$I = I_C \sin\gamma, \tag{2.5}$$

and

$$V = \varphi_0 \frac{\partial \gamma}{\partial t}. \tag{2.6}$$

These equations are known as the Josephson relations.

Note that the Josephson relations indicate that a Josephson junction can be seen as a non-linear inductor. Calculating the partial derivative of the current with respect to time, we find

$$\frac{\partial I}{\partial t} = \frac{\partial I}{\partial \gamma}\frac{\partial \gamma}{\partial t} = I_C \cos\gamma \cdot \frac{V}{\varphi_0}, \tag{2.7}$$

which can be rearranged to get the current-voltage relation of an inductor:

$$V = L(\gamma)\frac{\partial I}{\partial t}. \tag{2.8}$$

Here, $L(\gamma)$ is defined as

$$L(\gamma) = \frac{\varphi_0}{I_C \cos\gamma} = \frac{L_J}{\cos\gamma}. \tag{2.9}$$

which is the phase-dependent kinetic inductance of the Josephson junction. $L_J = \varphi_0/I_C$ is called the Josephson inductance.

In fabricated Josephson junctions, there is also a shunt capacitance present, which we can model with a capacitor with capacitance C_J in parallel with the junction itself. We define the Josephson charging energy, E_C, of a single Cooper pair as

$$E_C = \frac{(2e)^2}{2C_J}. \tag{2.10}$$

2.1.2 Superconducting Flux Qubits

Fundamentally, qubits are two-level quantum systems that can usually be manipulated and observed from the outside. Qubits are the basic building blocks used to implement quantum computers, and more recently, to probe the dynamics of various fundamental physics phenomena. In practice, achieving the necessary conditions to do quantum computing, such as long coherence times, accurate control and readout, and low susceptibility to environmental noise, is quite challenging. There are many different promising candidates for physical qubits, such as atoms, photons, quantum dots, and superconducting circuits based on Josephson junctions.

There are three main archetypes of superconducting qubits, namely the phase, charge, and flux qubits. The main distinguishing feature between these qubits is the regime they operate in, which depends on the ratio between the Josephson and charging energies E_J/E_C. A charge qubit operates in the charging regime where $E_J/E_C \ll 1$, whereas the flux and phase qubits operate in the flux/phase regime where $E_J/E_C \gg 1$.

In this section, we introduce the superconducting flux qubit, which is the archetype of the tunable ultrastrong coupling qubit used for the entanglement harvesting experiment.

The basic flux qubit, as shown in figure 2.2, is a superconducting loop with three Josephson junctions, with one of the junction being α $(0.5 < \alpha < 1)$ times the size than the other two.

Because the Cooper pairs in a superconductor can be described by a macroscopic wave function f $\psi = |\psi|e^{i\gamma}$ [3], the phase γ must be single-valued around a superconducting loop. This introduces a phase quantization constraint

$$\gamma_1 + \gamma_2 + \gamma_3 + 2\pi f = 2\pi n, \tag{2.11}$$

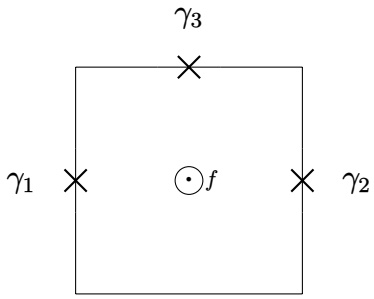

Figure 2.2: Circuit diagram of the basic flux qubit. The crosses in the figure represent Josephson junctions. An external magentic frustration f is applied to operate the flux qubit.

where γ_i is the phase drop across junction $i \in \{1,2,3\}$, $f = \Phi_{\text{ext}}/\Phi_0$ is the magnetic frustration, and $n \in \mathbb{Z}$.

Using equations (2.2) and (2.11), we can write down the potential of the system as

$$\frac{U_J}{E_J} = 2 + \alpha - \cos\gamma_1 - \cos\gamma_2 - \alpha\cos(\gamma_1 - \gamma_2 + 2\pi f), \tag{2.12}$$

assuming that the self-inductance of the loop L_g is much less than the Josephson inductance, and that $n = 0$. We can calculate the minima of the potential to give $\gamma_1 = -\gamma_2 = \pm\gamma^*$, with

$$\cos\gamma^* = \frac{1}{2\alpha}. \tag{2.13}$$

At the minima, the magnitude of the current is

$$I_p = I_C \sin\gamma^* = \pm I_C\sqrt{1 - \frac{1}{4\alpha^2}}, \tag{2.14}$$

which is the persistent current flowing in the qubit loop. The direction of this current depends on the phase, which can be controlled via the external flux Φ_{ext}.

We can write down the full quantum mechanical Hamiltonian of the system as [23]

$$\hat{H}_{\text{qb}} = \frac{1}{2}\left(\frac{\hat{P}_m^2}{M_m^2} + \frac{\hat{P}_p^2}{M_p^2}\right) + E_J\left(2 + \alpha - 2\cos\hat{\gamma}_-\cos\hat{\gamma}_+ - 2\cos(2\pi f + 2\hat{\gamma}_-)\right), \tag{2.15}$$

where we have promoted the phases $\hat{\gamma}_i$ to quantum operators, and we have defined $\hat{\gamma}_\pm = (\hat{\gamma}_1 \pm \hat{\gamma}_2)/2$. Because $E_J \gg E_C$, phase states are well-defined and we can use them as a basis to calculate the eigenstates, which can be solved numerically.

To recover the qubit behaviour of the flux qubit, we can approximate its two lowest levels by a two-level system using a tight-binding model [23]. Working with the persistent current basis $\{|\circlearrowleft\rangle, |\circlearrowright\rangle\}$, we can write the Hamiltonian of the effective two-level system as

$$\hat{H}_{\text{qb}} = -\frac{\epsilon}{2}\hat{\sigma}_z + \frac{\Delta}{2}\hat{\sigma}_x = \frac{1}{2}\begin{pmatrix} -\epsilon & \Delta \\ \Delta & \epsilon \end{pmatrix}, \tag{2.16}$$

where $\hat{\sigma}_x, \hat{\sigma}_y, \hat{\sigma}_z$ are the Pauli matrices,

$$\epsilon = 2I_p(\Phi_{\text{ext}} - \Phi_0/2) \tag{2.17}$$

is the magnetic energy of the system, and

$$\Delta \approx \frac{4E_J}{\sqrt{\alpha E_J/E_C}} e^{-0.15\sqrt{4\alpha(1+2\alpha)E_J/E_C}} \tag{2.18}$$

is the qubit gap. For a typical design, the qubit gap is in the order of a few GHz, which is accessible using existing microwave electronics equipment.

To diagonalize (2.16), we can apply a rotation

$$U = e^{-i\theta\hat{\sigma}_y} = \begin{pmatrix} \cos\frac{\theta}{2} & -\sin\frac{\theta}{2} \\ \sin\frac{\theta}{2} & \cos\frac{\theta}{2} \end{pmatrix} \tag{2.19}$$

where

$$\tan\theta = \frac{\Delta}{\epsilon} \tag{2.20}$$

so that the qubit Hamiltonian becomes

$$\hat{H}_{\text{qb}} = \frac{\sqrt{\epsilon^2 + \Delta^2}}{2}\hat{\sigma}_z \equiv \frac{\hbar\omega_q}{2}\hat{\sigma}_z \tag{2.21}$$

in the rotated basis $\{|e\rangle, |g\rangle\}$, where

$$|e\rangle = \cos\frac{\theta}{2}|\circlearrowleft\rangle + \sin\frac{\theta}{2}|\circlearrowright\rangle, \tag{2.22}$$

$$|g\rangle = \cos\frac{\theta}{2}|\circlearrowleft\rangle - \sin\frac{\theta}{2}|\circlearrowright\rangle. \tag{2.23}$$

These states can thus be identified as the ground and excited states of the qubit.

At the symmetry point, which is defined as the point with $\theta = \pi/2$, $|e\rangle$ and $|g\rangle$ are in superpositions of the persistent current states of equal magnitudes, so that the net current is zero and the qubit generates no magnetic flux.

On the other hand, when the qubit is biased far away from the symmetry point ($|\theta - \pi/2| \gg 0$), equations (2.22) and (2.23) show that the ground and excited states are effectively the two persistent current states. Thus we can see that, far away from the symmetry point, the qubit produces a nonzero magnetic flux with its sign dependent upon whether the qubit is excited. We can exploit this phenomenon to read out the state of the qubit by coupling the DC-SQUID to a readout resonator, so that the resonance frequency of the resonator shifts depending on the qubit state. This shift in resonance frequency can be detected, for example, by sending a microwave pulse at the unshifted resonance frequency into the resonator and then detecting the response from the resonator.

2.1.3 Qubit Control

Any arbitrary pure state of the qubit can be written as a superposition of the ground and excited basis vectors. Because only the relative phase between the coefficients of the basis vectors have meaning, and the state as unit norm, we can write such as state $|\psi\rangle$ as

$$|\psi\rangle = \cos\theta\,|g\rangle + e^{i\varphi}\sin\theta\,|e\rangle\,. \tag{2.24}$$

$|\psi\rangle$ can be represented as a point on a unit sphere, known as the Bloch sphere, as seen in figure 2.3.

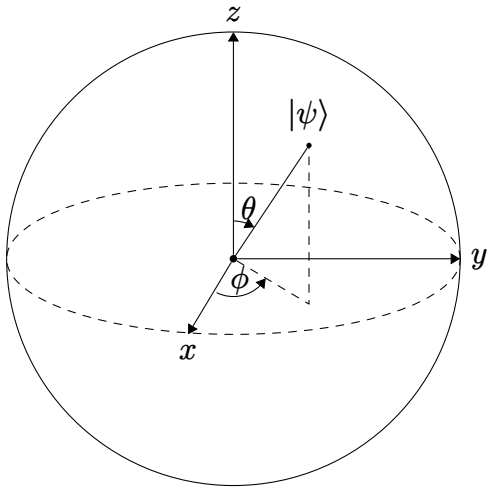

Figure 2.3: The Bloch sphere, with the qubit state $|\psi\rangle = \cos\theta\,|g\rangle + e^{i\varphi}\sin\theta\,|e\rangle$.

Controlling the qubit essentially means to rotate the qubit state vector around the Bloch sphere. More specifically, we have two types of rotations: first, rotations that change

the relative phase φ, called longitudinal rotations; second, rotations that change the qubit population θ, called transversal rotations. Longitudinal rotations can be implemented using the free precession of the qubit when placed in an external magnetic field. On the other hand, transversal rotations can be implemented with oscillatory external magnetic fields.

In the persistent current basis, we can write the Hamiltonian of an oscillating external magnetic field as

$$\hat{H}_{\mathrm{d}} = \frac{A}{2}\cos(\omega_d t + \phi)\hat{\sigma}_z, \tag{2.25}$$

where A is the amplitude of the driving magnetic field, ω_d is the driving frequency, and ϕ is the phase shift of the driving field. In the eigenbasis $\{|e\rangle, |g\rangle\}$ of the qubit, we have

$$\hat{H}_{\mathrm{d}} = \frac{A}{2}\cos(\omega_d t + \phi)\left(\frac{\epsilon}{\hbar\omega_q}\hat{\sigma}_z - \frac{\Delta}{\hbar\omega_q}\hat{\sigma}_x\right). \tag{2.26}$$

In order to get a time-independent Hamiltonian, we can rotate the system Hamiltonian $\hat{H} = \hat{H}_{\mathrm{qb}} + \hat{H}_d$ with $U = \exp(i\omega_d t\hat{\sigma}_z/2)$, and apply the rotating wave approximation (RWA), to find that

$$\hat{H}_{\mathrm{RWA}} = \frac{\hbar(\omega_q - \omega_d)}{2}\hat{\sigma}_z - \frac{A\Delta}{4\hbar\omega}\left(\cos\phi\hat{\sigma}_x - \sin\phi\hat{\sigma}_y\right). \tag{2.27}$$

Here we can see that the phase shift ϕ determines the rotation axis of the rotation applied, and that when $\omega_d = \omega_q$, the qubit frequency, the qubit rotates purely transversely at a rate

$$\Omega_R = 2\frac{A\Delta}{4\hbar^2\omega_q}, \tag{2.28}$$

which is called the Rabi frequency [6]. Thus, we can implement arbitrary longitudinal rotations by varying the phase shift ϕ and the total applied time of the external driving field.

2.1.4 Qubit Readout

In section 2.1.2, we noted that to implement the readout of a flux qubit, we can exploit the fact that, when a flux qubit is biased far away from the symmetry point, it produces a magnetic flux with a sign dependent on the state of the qubit. The detection of the sign of the flux is done in practice using a superconducting device called a DC-SQUID, where SQUID is an acronym for Superconducting QUantum Interference Device [15].

A schematic of the DC-SQUID is given in figure 2.4. Essentially, a DC-SQUID is a superconducting loop with two Josephson junctions in parallel. To operate the DC-SQUID,

a constant biasing current I_b is applied across the loop. Without any external field applied to the loop, the current splits evenly into the two branches. When an external field is applied, a circulating current I_{circ} is developed and the total induced currents of the two junctions become $I_b/2 \pm I_{\text{circ}}$. Whenever the magnitude of either of the induced currents becomes larger than I_c, the critical current of the junction, a voltage develops across the junction, and thus, by measuring the voltage across the DC-SQUID, we can obtain the sign and the magnitude of the external field, with a periodicity of $\Phi_0/2$.

Note that when a voltage is develops across the DC-SQUID, the DC-SQUID becomes resistive and enters the dissipative regime [19]. This causes the generation of quasiparticles, which in turn increases the decoherence rate of the qubit. Furthermore, in this regime the DC-SQUID emits microwave signals with broad spectral bandwidth that could potentially disturb the qubit.

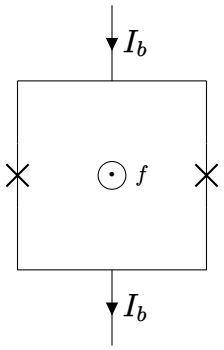

Figure 2.4: Circuit diagram of the DC-SQUID. A biasing current I_b is applied to operate the DC-SQUID.

There is an alternative mode of operation for the DC-SQUID, namely the inductive mode, in which the dissipative state is avoided [18,19]. In this mode, we exploit the property that the DC-SQUID acts like a non-linear inductor with its inductance dependent on the external magnetic flux. Using this, We can detect the qubit state via the impedance shift of the DC-SQUID.

2.2 Quantization of the Transmission Line

In this section, we introduce the transmission line and its quantization. The entanglement harvesting experiment relies on the ability for two qubits to couple simultaneously to a

one-dimensional scalar field [27, 28]. This one-dimensional scalar field can be conveniently provided by a transmission line, as we will see below.

A transmission line is a waveguide designed to allow arbitrary electromagnetic waves to travel long distances with minimal decay or distortion. On a superconducting chip, transmission lines are typically realized as coplanar waveguides, which consists of a center conductor between two ground planes at some distance apart. The gaps can be adjusted to achieve the desired impedance for the transmission line.

The transmission line is typically modelled by a long series of infinitesimally short segments, each of which containing a series inductor and a shunt capacitance, representing the distributed inductance and capacitance present in the transmission line. Figure 2.5 shows a few of these sections in series. Because we are working with superconducting transmission lines, we can ignore any resistances in our model.

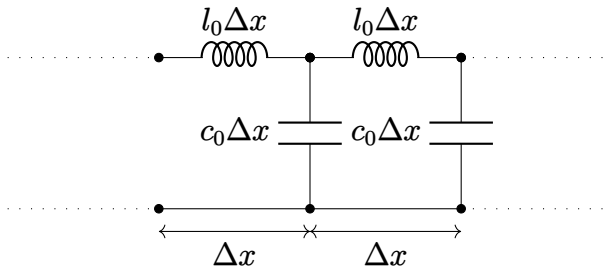

Figure 2.5: Circuit model of a short section of a transmission line.

Applying Kirchhoff's laws to a single section, we find that

$$V(x+\Delta x,t) = V(x,t) - l_0 \frac{\partial I(x,t)}{\partial t}\Delta x, \tag{2.29}$$

$$I(x+\Delta x,t) = I(x,t) - c_0 \frac{\partial V(x,t)}{\partial t}\Delta x. \tag{2.30}$$

In the continuum limit $\Delta x \to 0$, we obtain

$$\frac{\partial V(x,t)}{\partial x} = -l_0 \frac{\partial I(x,t)}{\partial t}, \tag{2.31}$$

$$\frac{\partial I(x,t)}{\partial x} = -c_0 \frac{\partial V(x,t)}{\partial t}. \tag{2.32}$$

These equations are known as the telegrapher's equations.

To proceed with quantization, we will first write down the Lagrangian and the Hamiltonian of the transmission line.

When working with the Lagrangian and Hamiltonian formulations, it is convenient to use the flux node variable

$$\Phi(x,t) = \int_{-\infty}^{t} \mathrm{d}\tau\, V(x,\tau). \tag{2.33}$$

Note that the voltage and current are related to Φ by

$$V(x,t) = \dot{\Phi}(x,t), \tag{2.34}$$

$$I(x,t) = -\frac{1}{l_0}\frac{\partial \Phi(x,t)}{\partial x}. \tag{2.35}$$

We can write the Lagrangian density as

$$\mathcal{L}(x,t) = \frac{c_0}{2}\left(\dot{\Phi}(x,t)\right)^2 - \frac{1}{2l_0}\left(\frac{\partial \Phi(x,t)}{\partial x}\right)^2, \tag{2.36}$$

and the Lagrangian is simply

$$L = \int_{-\infty}^{\infty} \mathrm{d}x\, \mathcal{L}(x,t). \tag{2.37}$$

The Euler-Lagrange equation

$$\frac{\mathrm{d}}{\mathrm{d}t}\frac{\partial \mathcal{L}}{\partial \dot{\Phi}} - \frac{\partial \mathcal{L}}{\partial \Phi} = 0 \tag{2.38}$$

applied to (2.36) becomes

$$c_0 \ddot{\Phi}(x,t) - \frac{1}{l_0}\frac{\partial^2 \Phi(x,t)}{\partial x^2} = 0. \tag{2.39}$$

We recognize this equation as the wave equation of the flux. Alternatively, this equation is known as the Klein-Gordon equation for a freely propagating 1D scalar field in quantum field theory. We can now see that transmission lines can provide the necessary interaction field for the qubits for an entanglement harvesting experiment.

To solve this equation, we first write the ansatz as a plane waves expansion:

$$\Phi(x,t) = \frac{1}{N}\sum_k \Phi_k(t) e^{ikx}, \tag{2.40}$$

where N is a normalization constant. Suppose that the transmission line is of length L; then the wavevector k is discretized in units $k = 2\pi m/L$, $m \in \mathbb{Z}$.

For a single mode k, the wave equation becomes

$$\ddot{\Phi}_k(t) + \omega_k^2 \Phi_k(t) = 0, \tag{2.41}$$

where we have defined

$$\omega_k = |k| v, \tag{2.42}$$

$$v = \frac{1}{\sqrt{c_0 l_0}}, \tag{2.43}$$

as the frequency and speed of light in the transmission line respectively. The general solution to equation (2.41) is $\Phi_k(t) = c_k e^{-i\omega_k t} + c_{-k}^* e^{i\omega_k t}$; so that

$$\Phi(x,t) = \frac{1}{N} \sum_k \left(c_k e^{i(kx - \omega_k t)} + \text{c.c.} \right). \tag{2.44}$$

Now we can calculate the conjugate momentum of the flux, the charge density $q(x,t) = c_0 \dot{\Phi}(x,t)$, as

$$q(x,t) = \frac{i c_0}{N} \sum_k \omega_k (-c_k e^{i(kx - \omega_k t)} + \text{c.c.}). \tag{2.45}$$

Through a Legendre transform, we find the Hamiltonian to be

$$\begin{aligned} H &= \int_0^L \mathrm{d}x \left(\frac{1}{2c_0} q^2(x,t) + \frac{1}{2l_0} \left(\frac{\partial \Phi(x,t)}{\partial x} \right)^2 \right) \\ &= \frac{1}{2N^2} \sum_k \left(c_0 \omega_k^2 (2|c_k|^2 L) + \frac{1}{l_0} (2k^2 |c_k|^2 L) \right) \\ &= \frac{L c_0}{N^2} 2 \sum_k \omega_k^2 |c_k|^2 \\ &= 2 \sum_k \omega_k^2 |c_k|^2, \end{aligned} \tag{2.46}$$

where for the last equality we've set the normalization constant to be $N = \sqrt{L c_0}$.

Defining amplitudes $A_k = \sqrt{2} \omega_k c_k$ we can write

$$H = \frac{1}{2} \left(A_k A_k^* + A_k^* A_k \right) \tag{2.47}$$

which has the form of a simple harmonic oscillator. Moreover, we have

$$\Phi(x,t) = \frac{1}{\sqrt{2Lc_0}} \sum_k \frac{1}{\omega_k} \left(A_k^* e^{i(\omega_k t - kx)} + \text{c.c.} \right), \tag{2.48}$$

$$q(x,t) = \sqrt{\frac{c_0}{2L}} \sum_k \left(i A_k^* e^{i(\omega_k t - kx)} + \text{c.c.} \right). \tag{2.49}$$

We can now apply canonical quantization to the Hamiltonian. The first step of canonical quantization is to promote the canonically conjugate variables to quantum operators. As $\{\Phi(x,t), q(x,t)\}$ are the canonically conjugate variables for the transmission line, we promote them to quantum operators obeying the commutation relation

$$[\hat{\Phi}(x,t), \hat{q}(x,t)] = i\hbar\delta(x - x'). \tag{2.50}$$

From equations (2.48) and (2.49), we find that

$$[\hat{A}_k, \hat{A}_{k'}^\dagger] = \hbar\omega_k \delta_{kk'}. \tag{2.51}$$

From this we can identify $\hat{A}_k = \sqrt{\hbar\omega_k}\hat{b}_k$, where $\hat{b}_k$ is the photon annihilation operator in mode k. Substituting into (2.47), we get

$$\hat{H} = \sum_k \hbar\omega_k \left(\hat{b}_k^\dagger \hat{b}_k + \frac{1}{2} \right) \tag{2.52}$$

which is the sum of quantum harmonic oscillators corresponding to different modes k.

Finally, we can write the quantized flux field as

$$\hat{\Phi}(x,t) = \frac{1}{\sqrt{L}} \sum_k \sqrt{\frac{\hbar}{2c_0\omega_k}} \left(\hat{b}_k^\dagger e^{i(\omega_k t - kx)} + \text{h.c.} \right). \tag{2.53}$$

2.3 The Unruh-DeWitt Model

The Unruh-DeWitt (UdW) detector model is an idealized model that captures the essence of light-matter interaction, where a monopole detector is coupled to a massless scalar field [20]. This model is commonly used to study the entanglement effects in relativistic quantum information (RQI), including entanglement harvesting.

The monopole detector in a UdW model is usually a qubit with ground and excited states $|g\rangle$ and $|e\rangle$ respectively, with energy gap $\hbar\Omega$. For $n+1$ dimensional spacetime, the detector is coupled to the scalar field $\hat{\phi}$ via the interaction Hamiltonian

$$\hat{H}_I(t) = \lambda\chi(t)\hat{\mu}(t)\int \mathrm{d}^n\mathbf{x}\, F(\mathbf{x}-\mathbf{x}_0)\hat{\phi}(\mathbf{x},t). \tag{2.54}$$

where λ is the maximum coupling strength, $\chi(t)$ is a switching function that turns on coupling for a period of time with $|\chi(t)|\leq 1$ for all t, $F(\mathbf{x})$ is the spatial smearing function that encodes the shape of the detector, $\mathbf{x}_0$ is the center position of the qubit, and

$$\hat{\mu}(t) = \hat{\sigma}^+ e^{i\Omega t} + \hat{\sigma}^- e^{-i\Omega t} \tag{2.55}$$

is the monopole moment of the detector, with $\hat{\sigma}_+ = |e\rangle\langle g|$ and $\hat{\sigma}_- = |g\rangle\langle e|$.

A $n+1$ dimensional massless scalar field is governed by the Klein-Gordon equation [26]

$$\left(\frac{1}{c^2}\frac{\partial^2}{\partial t^2} - \nabla^2\right)\phi(x,t) = 0. \tag{2.56}$$

If we solve it and quantize the solution, we obtain

$$\hat{\phi}(\mathbf{x},t) = \int \frac{\mathrm{d}^n\mathbf{k}}{\sqrt{(2\pi)^n 2\omega_{\mathbf{k}}}}\left(\hat{a}^\dagger_{\mathbf{k}} e^{i(\omega_{\mathbf{k}}t - \mathbf{k}\cdot\mathbf{x})} + \text{h.c.}\right). \tag{2.57}$$

Its conjugate momentum, which is defined as $\hat{\pi}(\mathbf{x},t) = \partial_t\hat{\phi}(\mathbf{x},t)$, can be calculated as

$$\hat{\pi}(\mathbf{x},t) = \int \frac{\mathrm{d}^n\mathbf{k}}{\sqrt{2(2\pi)^n}}\sqrt{\omega_{\mathbf{k}}}\left(i\hat{a}^\dagger_{\mathbf{k}} e^{i(\omega_{\mathbf{k}}t - \mathbf{k}\cdot\mathbf{x})} + \text{h.c.}\right). \tag{2.58}$$

As we will see in section 3.1, the interaction field of a flux qubit coupled to a transmission line is in fact the $1+1$ dimensional conjugate momentum $\hat{\pi}(x,t)$ of the scalar field $\hat{\phi}(x,t)$, rather than the scalar field itself.

Chapter 3

Entanglement Harvesting With Superconducting Flux Qubits

Recent studies [27, 28, 31] in relativistic quantum information have predicted that it is possible to entangle two qubits tunably coupled to the same quantum field in its vacuum state, by allowing the qubits to couple to the field for a very short amount of time, even if the coupling time forbids the formation of a lightlike connection between the qubits. This is possible due to the correlations already present in the vacuum field. In this chapter, we seek to understand the conditions required to demonstrate this phenomenon with our current experimental hardware.

This chapter is organized as follows. In section 3.1, we derive the form of coupling between flux qubits and a transmission line, and we relate it to the Unruh-DeWitt model. In section 3.2, we use a perturbative approach to derive the formulae of the expected amount of entanglement that we can harvest with flux qubits coupled to a transmission line. Finally, in section 3.3, we calculate the entanglement using parameters faithful to our experimental setup.

3.1 Flux Qubit Coupled to a Transmission Line

In this section, we derive the coupling Hamiltonian between a flux qubit and an open transmission line using the circuit quantization method introduced in [25].

The circuit model is shown in figure 3.1, where the flux qubit is coupled through its γ_β junction to an open transmission line. We can write the Hamiltonian of this lumped

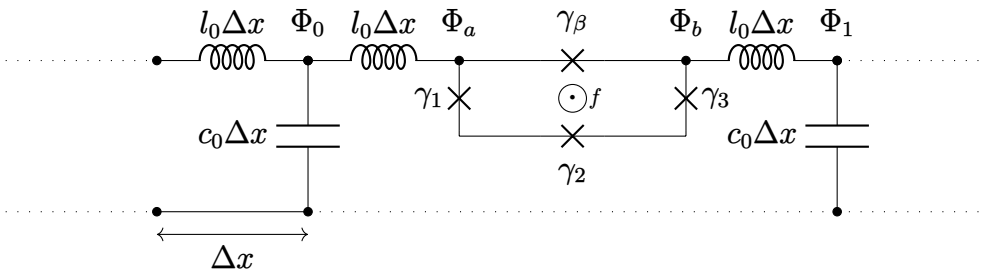

Figure 3.1: Circuit model of a four-junction persistent current flux qubit glavanically coupled to an open transmission line. The qubit shares the β junction with the transmission line.

element circuit as

$$\hat{H} = \sum_{i=0}^{N} \frac{\hat{q}_i^2}{2\Delta x\, c_0} + \sum_{i=1}^{N-1} \frac{(\hat{\Phi}_{i+1} - \hat{\Phi}_i)^2}{2\Delta x\, l_0} + \frac{(\hat{\Phi}_1 - \hat{\Phi}_b)^2 + (\hat{\Phi}_a - \hat{\Phi}_0)^2}{\Delta x\, l_0} + \hat{H}_{\mathrm{qb}}, \tag{3.1}$$

where c_0 and l_0 are the capacitance and inductance per unit length of the transmission line respectively, Δx is the length of each lumped element oscillator, and $\hat{H}_{\mathrm{qb}}$ is the qubit Hamiltonian. We can rewrite (3.1) with a change of variable

$$\hat{\Phi}_\pm = \hat{\Phi}_b \pm \hat{\Phi}_a \tag{3.2}$$

to obtain

$$\hat{H} = \Delta x \sum_{i=0}^{N} \left[\frac{1}{2c_0} \left(\frac{\hat{q}_i}{\Delta x} \right)^2 + \frac{1}{2l_0} \left(\frac{\hat{\Phi}_{i+1} - \hat{\Phi}_i}{\Delta x} \right)^2 \right] + \frac{[(\hat{\Phi}_1 + \hat{\Phi}_0) - \hat{\Phi}_+]^2}{2\Delta x\, l_0} + \frac{(\hat{\Phi}_1 - \hat{\Phi}_0)\hat{\Phi}_-}{\Delta x\, l_0} + \hat{H}_{\mathrm{qb}}. \tag{3.3}$$

Letting $\Delta x \to 0$, we find that in the continuum limit

$$\hat{H} = \int_{-\infty}^{\infty} \mathrm{d}x \left[\frac{\hat{q}^2(x)}{2c_0} + \frac{\partial_x \hat{\Phi}^2(x)}{2l_0} + \delta(x) \frac{1}{l_0} \partial_x \hat{\Phi}(x) \cdot \hat{\Phi}_- \right] + \frac{\hat{\Phi}_-^2}{2l_0\, \mathrm{d}x} + \hat{H}_{\mathrm{qb}}. \tag{3.4}$$

Note that we have eliminated the third term since $(\hat{\Phi}_1 + \hat{\Phi}_0) - \hat{\Phi}_+ \to 0$ as $\Delta x \to 0$.

Noting that the current in the transmission line is related to the flux by the relation

$$\hat{I}(x) = -\frac{1}{l_0} \partial_x \hat{\Phi}(x), \tag{3.5}$$

we can see that the third term in (3.4) effectively couples the current to the flux drop $\hat{\Phi}_-$ across the qubit. As the flux qubit operates on the flux jump of the β junction, this term represents the interaction Hamiltonian between the qubit and the transmission line.

The second last term in (3.4) is a qubit renormalization term, which occurs commonly in spin-boson models. Writing the flux jump operator as $\hat{\Phi}_- = \varphi_0 \hat{\gamma}_\beta$, and replacing the inductance term $l_0\,\mathrm{d}x$ with Z_0/ω, we find that this renormalization term is of the order

$$\hat{H}_{\text{renorm}} \sim \frac{\hbar^2 \omega}{16 Z_0 e^2} \hat{\gamma}_\beta^2. \tag{3.6}$$

Taking the typical values in a superconducting setup, $Z_0 = 50\ \Omega$ and $\omega = 2\pi \cdot 5$ GHz, we find that its magnitude is around $H_{\text{renorm}}/\hbar \approx 161\ \text{GHz} \cdot \gamma_\beta^2$. Compared to the qubit potential $U = E_J(1 - \cos\gamma_\beta)$, where $E_J/\hbar$ is in the order of 800 GHz, we can see that this renormalization is relatively small and can be ignored.

Lastly, let us derive the quantized current $\hat{I}(x,t)$, which is coupled to the qubit:

$$\begin{aligned}
\hat{I}(x,t) &= -\frac{1}{l_0}\partial_x \hat{\Phi}(x,t) \\
&= -\frac{1}{l_0\sqrt{L}} \sum_k \sqrt{\frac{\hbar}{2c_0|k|}} \left(ik \hat{b}_k e^{i(kx - |k|t)} + \text{h.c.} \right) \\
&= -\frac{1}{\sqrt{L}} \sqrt{\frac{L}{2\pi}} \sum_k \Delta k \sqrt{\frac{\hbar v}{2l_0}} \frac{k}{\sqrt{|k|}} \left(\frac{i}{\sqrt{\Delta k}} \hat{b}_k e^{i(kx - |k|t)} + \text{h.c.} \right),
\end{aligned} \tag{3.7}$$

with $\Delta k = 2\pi/L$.

In order to recover the current equation of an infinite transmission line, we let $L \to \infty$, so that $\Delta k \to 0$; we get

$$\hat{I}(x,t) = -\sqrt{\frac{\hbar v}{l_0}} \int_{-\infty}^{\infty} \mathrm{d}k\, \frac{1}{2\sqrt{\pi}} \frac{k}{\sqrt{|k|}} \left(i \hat{a}_k e^{i(kx - |k|t)} + \text{h.c.} \right), \tag{3.8}$$

where we have defined $\hat{a}_k = \lim_{\Delta k \to 0} \hat{b}_k / \sqrt{\Delta k}$.

Comparing (3.8) with the conjugate momentum of the 1D scalar field, we can see that they are identical other than the constant factor outside the integral, and that we have $k/\sqrt{|k|}$ in the current rather than $\sqrt{|k|}$ in $\hat{\pi}$. Though, as it turns out, for the expressions we are interested in calculating in the next section, the $k/\sqrt{|k|}$ factor always appears squared;

and

$$\left(\frac{k}{\sqrt{|k|}}\right)^2 = \frac{k^2}{|k|} = |k| = (\sqrt{|k|})^2.$$

Hence for our purposes, the coupling model between the qubit and the transmission line is equivalent to the Unruh-DeWitt model with the massless field being the conjugate momentum $\hat{\pi}$ of the 1D Klein-Gordon scalar field. The extra constant before the integral can be absorbed into the coupling factor λ.

3.2 Perturbative Calculations

In this section, we adapt the derivations given in [27] and [31] to calculate the amount of entanglement generated using two superconducting flux qubits coupled to a transmission line at finite temperature. To simply the calculations, we will set $v = 1$ and $\hbar = 1$.

From the previous section, we found that the qubits couple to conjugate momentum $\hat{\pi}(x,t)$ of the (1+1)D scalar field. We now continue to calculate the amount of entanglement harvested by two qubits coupled to such a field using perturbation theory. First, we add a UV cutoff function $C_\xi(k)$ to the field:

$$\hat{\pi}(x,t) = \frac{1}{2\sqrt{\pi}} \int_{-\infty}^{\infty} \mathrm{d}k\, C_\xi(k) \sqrt{|k|} \left(i\hat{a}_k^\dagger e^{i(|k|t - kx)} + \text{h.c.} \right). \tag{3.9}$$

The interaction Hamiltonian is the UdW model applied to the two qubits:

$$\begin{aligned} \hat{H}_I(t) &= \sum_{\nu \in \{A,B\}} \lambda \mu_\nu(t) \chi_\nu(t) \int_{-\infty}^{\infty} \mathrm{d}x\, F_\nu(x - x_\nu) \hat{\pi}(x,t) \\ &= \sum_{\nu \in \{A,B\}} \lambda \mu_\nu(t) \chi_\nu(t) \int_{-\infty}^{\infty} \mathrm{d}k\, C_\xi(k) \sqrt{\frac{|k|}{2}} \left(i\hat{a}_k^\dagger e^{i(|k|t - kx_\nu)} \widetilde{F}_\nu(-k) + \text{h.c.} \right), \end{aligned} \tag{3.10}$$

where the monopole moment for qubit ν is

$$\mu_\nu(t) = |e_\nu\rangle\langle g_\nu|\, e^{i\Omega_\nu t} + |g_\nu\rangle\langle e_\nu|\, e^{-i\Omega_\nu t}, \tag{3.11}$$

$\chi_\nu(t)$ is a time-dependent switching function, and $F_\nu(x)$ is the spatial smearing function of qubit ν. Here, we defined the Fourier transform $\widetilde{f}(k)$ of an arbitrary function $f(x)$ as

$$\widetilde{f}(k) = \frac{1}{\sqrt{2\pi}} \int_{-\infty}^{\infty} \mathrm{d}x\, f(x) e^{ikx}. \tag{3.12}$$

We can write the time evolution operator $\hat{U}$ via a Dyson expansion:

$$\hat{U} = \mathbb{1} + \hat{U}^{(1)} + \hat{U}^{(2)} + \cdots, \tag{3.13}$$

where

$$\hat{U}^{(1)} = -i\int_{-\infty}^{\infty} \mathrm{d}t\, \hat{H}_I(t), \quad \hat{U}^{(2)} = -\int_{-\infty}^{\infty} \mathrm{d}t \int_{-\infty}^{t} \mathrm{d}t'\, \hat{H}_I(t)\hat{H}_I(t'). \tag{3.14}$$

Given the initial state $\hat{\rho}_0 = \hat{\rho}_\pi \otimes \hat{\rho}_{AB}^{(0)}$, the final state is given by $\hat{\rho} = \hat{U}\hat{\rho}_0\hat{U}^\dagger$. We are interested in the final state of the two qubits with the field traced out:

$$\hat{\rho}_{AB} = \mathrm{Tr}_{\hat{\pi}}[\hat{\rho}] = \mathrm{Tr}_{\hat{\pi}}[\hat{U}\hat{\rho}_0\hat{U}^\dagger]. \tag{3.15}$$

To this end, define

$$\hat{\rho}_{AB}^{(i,j)} = \mathrm{Tr}_{\hat{\pi}}\left[\hat{U}^{(i)}\hat{\rho}_0\hat{U}^{(j)\dagger}\right] \tag{3.16}$$

so that

$$\hat{\rho}_{AB} = \hat{\rho}_{AB}^{(0)} + \underbrace{\hat{\rho}_{AB}^{(1,0)} + \hat{\rho}_{AB}^{(0,1)}}_{\hat{\rho}_{AB}^{(1)}} + \underbrace{\hat{\rho}_{AB}^{(2,0)} + \hat{\rho}_{AB}^{(0,2)} + \hat{\rho}_{AB}^{(1,1)}}_{\hat{\rho}_{AB}^{(2)}} + O(\lambda^4). \tag{3.17}$$

Because we are tracing out the field $\hat{\pi}$, only the terms of $\hat{U}\hat{\rho}_0\hat{U}^\dagger$ that are diagonal in the field will be included in $\hat{\rho}_{AB}$. Consequently, if $\hat{\rho}_\pi$ is diagonal, which is the case for the scenarios we will be considering, then $\hat{\rho}_{AB}^{(i,j)} = 0$ when i, j have different parities. Hence, we only need to calculate $\hat{\rho}_{AB}^{(2)}$ in (3.17) in order to obtain the final density matrix up to λ^2.

Using equations (3.10) and (3.14), we find that [27]

$$\begin{aligned}\hat{\rho}_{AB}^{(2)} = \sum_{\nu,\eta\in\{A,B\}} \lambda^2 \Big[&\int_{-\infty}^{\infty} \mathrm{d}t \int_{-\infty}^{\infty} \mathrm{d}t'\, \chi_\nu(t')\chi_\eta(t)\hat{\mu}_\nu(t')\hat{\rho}_{AB}^{(0)}\hat{\mu}_\eta(t) W(x_\eta, t, x_\nu, t') \\ &- \int_{-\infty}^{\infty} \mathrm{d}t \int_{-\infty}^{t} \mathrm{d}t'\, \chi_\nu(t)\chi_\eta(t')\hat{\mu}_\nu(t)\hat{\mu}_\eta(t')\hat{\rho}_{AB}^{(0)} W(x_\nu, t, x_\eta, t') \\ &- \int_{-\infty}^{\infty} \mathrm{d}t \int_{-\infty}^{t} \mathrm{d}t'\, \chi_\nu(t)\chi_\eta(t')\hat{\rho}_{AB}^{(0)}\hat{\mu}_\eta(t')\hat{\mu}_\nu(t) W(x_\eta, t', x_\nu, t) \Big],\end{aligned} \tag{3.18}$$

where

$$W(x_\nu, t, x_\eta, t') = \int_{-\infty}^{\infty} \mathrm{d}x \int_{-\infty}^{\infty} \mathrm{d}x' F_\nu(x - x_\nu) F_\eta(x' - x_\eta)\, \mathrm{Tr}_{\hat{\pi}}\left[\hat{\pi}(x,t)\hat{\pi}(x',t')\hat{\rho}_\pi\right] \tag{3.19}$$

is the two-point correlator.

Let's consider the case where the field is in a thermal state with temperature $T_{\rm th}$:

$$\hat{\rho}_\pi = \frac{e^{-\beta \hat{H}_\pi}}{\mathcal{Z}}, \tag{3.20}$$

where $\hat{H}_\pi = \int \mathrm{d}k\, |k| \hat{a}_k^\dagger \hat{a}_k$, $\beta = 1/k_B T_{\rm th}$, and $\mathcal{Z} = \mathrm{Tr}\left[e^{-\beta \hat{H}_\pi}\right]$.

Now, making use of the identities $e^{-\beta \hat{H}_\pi} \hat{a}_k e^{\beta \hat{H}_\pi} = e^{\beta |k|} \hat{a}_k$ and $[\hat{a}_k, \hat{a}_{k'}^\dagger] = \delta(k - k')$, we can calculate [31]

$$\mathrm{Tr}_{\hat{\pi}}[\hat{\rho}_\pi \hat{a}_k \hat{a}_{k'}^\dagger] = e^{\beta |k|} \left(\mathrm{Tr}_{\hat{\pi}}[\hat{\rho}_\pi \hat{a}_k \hat{a}_{k'}^\dagger] + \delta(k - k') \right);$$

from which we obtain

$$\mathrm{Tr}_{\hat{\pi}}[\hat{\rho}_\pi \hat{a}_k \hat{a}_{k'}^\dagger] = \frac{e^{\beta |k|}}{e^{\beta |k|} - 1} \delta(k - k'). \tag{3.21}$$

Similarly, we find that

$$\mathrm{Tr}_{\hat{\pi}}[\hat{\rho}_\pi \hat{a}_k^\dagger \hat{a}_{k'}] = \frac{1}{e^{\beta |k|} - 1} \delta(k - k'), \tag{3.22}$$

$$\mathrm{Tr}_{\hat{\pi}}[\hat{\rho}_\pi \hat{a}_k \hat{a}_{k'}] = 0, \tag{3.23}$$

$$\mathrm{Tr}_{\hat{\pi}}[\hat{\rho}_\pi \hat{a}_k^\dagger \hat{a}_{k'}^\dagger] = 0. \tag{3.24}$$

Next, using the identities above, we can compute the two-point function $w(x, t, x', t') = \mathrm{Tr}[\hat{\rho}_\pi \hat{\pi}(x, t) \hat{\pi}(x', t')]$ to obtain

$$w(x, t, x', t') = w^{\rm vac}(x, t, x', t') + w_\beta^{\rm th}(x, t, x', t'), \tag{3.25}$$

where

$$w^{\rm vac}(x, t, x', t') = \int_{-\infty}^{\infty} \frac{\mathrm{d}k}{4\pi} |k| C_\xi^2(k) e^{-i|k|(t - t')} e^{ik(x - x')}, \tag{3.26}$$

$$w_\beta^{\rm th}(x, t, x', t') = \int_{-\infty}^{\infty} \frac{\mathrm{d}k}{4\pi (e^{\beta |k|} - 1)} |k| C_\xi^2(k) \left(e^{i|k|(t - t')} e^{-ik(x - x')} + \text{c.c.} \right) \tag{3.27}$$

are the vacuum and thermal contributions to the two-point function respectively.

We can now calculate $\hat{\rho}_{AB} = \hat{\rho}_{AB}^{(0)} + \hat{\rho}_{AB}^{(2)} + O(\lambda^4)$. First, let us consider when the two qubits are prepared in their ground states: $\hat{\rho}_{AB}^{(0)} = |gg\rangle\langle gg|$. Combining (3.18), (3.19), and (3.25), we end up with

$$\hat{\rho}_{AB}^{gg} = \begin{pmatrix} 1 - \mathcal{L}_{AA}^{(+,+)} - \mathcal{L}_{BB}^{(+,+)} & 0 & 0 & \left(\mathcal{M}^{(+,+)}\right)^* \\ 0 & \mathcal{L}_{AA}^{(+,+)} & \mathcal{L}_{AB}^{(+,+)} & 0 \\ 0 & \left(\mathcal{L}_{AB}^{(+,+)}\right)^* & \mathcal{L}_{BB}^{(+,+)} & 0 \\ \mathcal{M}^{(+,+)} & 0 & 0 & 0 \end{pmatrix} + O(\lambda^4), \tag{3.28}$$

where the matrix is written in the basis $\{|g_A\rangle|g_B\rangle\,, |e_A\rangle|g_B\rangle\,, |g_A\rangle|e_B\rangle\,, |e_A\rangle|e_B\rangle\}$, and

$$\mathcal{L}_{\nu\eta}^{(s_A,s_B)} = \mathcal{L}_{\nu\eta,\,\mathrm{vac}}^{(s_A,s_B)} + 2\pi\lambda^2 \int_{-\infty}^{\infty} \mathrm{d}k \left\{ \frac{|k|}{2} \frac{C_\xi^2(k)\widetilde{F}_\nu^*(k)\widetilde{F}_\eta(k)e^{-ik(x_\nu - x_\eta)}}{e^{\beta|k|}-1} \right. \\ \left. \cdot \left[\widetilde{\chi}_\nu^*(|k|-s_\nu\Omega_\nu)\widetilde{\chi}_\eta(|k|-s_\eta\Omega_\eta) + \widetilde{\chi}_\nu(|k|+s_\nu\Omega_\nu)\widetilde{\chi}_\eta^*(|k|+s_\eta\Omega_\eta)\right] \right\}, \tag{3.29}$$

$$\mathcal{M}^{(s_A,s_B)} = \mathcal{M}_{\mathrm{vac}}^{(s_A,s_B)} - 2\pi\lambda^2 \int_{-\infty}^{\infty} \mathrm{d}k \left\{ \frac{|k|}{2} \frac{C_\xi^2(k)\widetilde{F}_A(k)\widetilde{F}_B^*(k)e^{ik(x_A - x_B)}}{e^{\beta|k|}-1} \right. \\ \left. \cdot \left[\widetilde{\chi}_A^*(|k|-s_A\Omega_A)\widetilde{\chi}_B(|k|+s_B\Omega_B) + \widetilde{\chi}_A(|k|+s_A\Omega_A)\widetilde{\chi}_B^*(|k|-s_B\Omega_B)\right] \right\}, \tag{3.30}$$

with $s_A, s_B \in \{-1, 1\}$; and

$$\mathcal{L}_{\nu\eta,\,\mathrm{vac}}^{(s_A,s_B)} = 2\pi\lambda^2 \int_{-\infty}^{\infty} \mathrm{d}k\, \frac{|k|}{2} C_\xi^2(k)\widetilde{F}_\nu^*(k)\widetilde{F}_\eta(k)e^{-ik(x_\nu - x_\eta)}\widetilde{\chi}_\nu(|k|+s_\nu\Omega_\nu)\widetilde{\chi}_\eta^*(|k|+s_\eta\Omega_\eta), \tag{3.31}$$

$$\mathcal{M}_{\mathrm{vac}}^{(s_A,s_B)} = -\lambda^2 \int_{-\infty}^{\infty} \mathrm{d}k \int_{-\infty}^{\infty} \mathrm{d}t \int_{-\infty}^{t} \mathrm{d}t'\, e^{-i|k|(t-t')} C_\xi^2(k) \\ \cdot \left[\widetilde{F}_A(k)\widetilde{F}_B^*(k)e^{ik(x_A - x_B)}\chi_A(t)\chi_B(t')e^{i(s_A\Omega_A t + s_B\Omega_B t')} + (A \leftrightarrow B)\right]. \tag{3.32}$$

Similarly, for $\hat{\rho}_{AB}^{(0)} \in \{|eg\rangle\langle eg|\,, |ge\rangle\langle ge|\,, |ee\rangle\langle ee|\}$, we get

$$\hat{\rho}_{AB}^{eg} = \begin{pmatrix} \mathcal{L}_{AA}^{(-,+)} & 0 & 0 & \mathcal{L}_{AB}^{(-,+)} \\ 0 & 1 - \mathcal{L}_{AA}^{(-,+)} - \mathcal{L}_{BB}^{(-,+)} & \left(\mathcal{M}^{(-,+)}\right)^* & 0 \\ 0 & \mathcal{M}^{(-,+)} & 0 & 0 \\ \left(\mathcal{L}_{AB}^{(-,+)}\right)^* & 0 & 0 & \mathcal{L}_{BB}^{(-,+)} \end{pmatrix} + O(\lambda^4), \tag{3.33}$$

$$\hat{\rho}_{AB}^{ge} = \begin{pmatrix} \mathcal{L}_{BB}^{(+,-)} & 0 & 0 & \left(\mathcal{L}_{AB}^{(+,-)}\right)^* \\ 0 & 0 & \mathcal{M}^{(+,-)} & 0 \\ 0 & \left(\mathcal{M}^{(+,-)}\right)^* & 1 - \mathcal{L}_{AA}^{(+,-)} - \mathcal{L}_{BB}^{(+,-)} & 0 \\ \mathcal{L}_{AB}^{(+,-)} & 0 & 0 & \mathcal{L}_{AA}^{(+,-)} \end{pmatrix} + O(\lambda^4), \tag{3.34}$$

$$\hat{\rho}^{ee}_{AB} = \begin{pmatrix} 0 & 0 & 0 & \mathcal{M}^{(-,-)} \\ 0 & \mathcal{L}^{(-,-)}_{BB} & \left(\mathcal{L}^{(-,-)}_{AB}\right)^* & 0 \\ 0 & \mathcal{L}^{(-,-)}_{AB} & \mathcal{L}^{(-,-)}_{AA} & 0 \\ \left(\mathcal{M}^{(-,-)}\right)^* & 0 & 0 & 1 - \mathcal{L}^{(-,-)}_{AA} - \mathcal{L}^{(-,-)}_{BB} \end{pmatrix} + O(\lambda^4). \tag{3.35}$$

In general, for the case where the qubits are in thermal equilibrium, we can take the initial state as

$$\begin{aligned} \hat{\rho}^{(0)}_{AB} &= (p_A \left|g_A\right\rangle\!\left\langle g_A\right| + (1-p_A) \left|e_A\right\rangle\!\left\langle e_A\right|) \otimes (p_B \left|g_B\right\rangle\!\left\langle g_B\right| + (1-p_B) \left|e_B\right\rangle\!\left\langle e_B\right|) \\ &= p_A p_B \left|gg\right\rangle\!\left\langle gg\right| + (1-p_A) p_B \left|eg\right\rangle\!\left\langle eg\right| + p_A (1-p_B) \left|ge\right\rangle\!\left\langle ge\right| + (1-p_A)(1-p_B) \left|ee\right\rangle\!\left\langle ee\right|, \end{aligned} \tag{3.36}$$

where $p_A, p_B \in [0,1]$ are the ground state populations of qubits A and B, respectively. The final evolved state would then become

$$\hat{\rho}_{AB} = p_A p_B \hat{\rho}^{gg}_{AB} + (1-p_A) p_B \hat{\rho}^{eg}_{AB} + p_A (1-p_B) \hat{\rho}^{ge}_{AB} + (1-p_A)(1-p_B) \hat{\rho}^{ee}_{AB}. \tag{3.37}$$

Finally, to quantify the amount of entanglement harvested, we can calculate the concurrence [12] of this state. The concurrence of density matrices with the form

$$\hat{\rho} = \begin{pmatrix} \rho_{11} & 0 & 0 & \rho_{14} \\ 0 & \rho_{22} & \rho_{23} & 0 \\ 0 & \rho^*_{23} & \rho_{33} & 0 \\ \rho^*_{14} & 0 & 0 & \rho_{44} \end{pmatrix} \tag{3.38}$$

is given by [33]

$$C(\hat{\rho}) = 2 \max\{|\rho_{23}| - \sqrt{\rho_{11}\rho_{44}}, |\rho_{14}| - \sqrt{\rho_{22}\rho_{33}}, 0\}. \tag{3.39}$$

The concurrence is an entanglement monotone—a non-negative function that quantifies the amount of entanglement in a state [13]. The concurrence of a separable state $\hat{\rho}$ is always 0. Note that, although the form given in (3.39) requires terms of order λ^4 in general, the contribution is not likely to be significant for the cases that we consider.

To proceed further, we will have to specialize the various functions used in the integrals. First, we use a Gaussian smearing function as the spatial smearing function for both qubits:

$$F_\nu(x) = F(x) = \frac{1}{\sqrt{\pi}\sigma} e^{-x^2/\sigma^2}. \tag{3.40}$$

Moreover, we use Gaussian switching for both qubits, with a characteristic timescale of T:

$$\chi_\nu(t) = e^{-(t-t_\nu)^2/T^2}. \tag{3.41}$$

The Gaussian switching function is found in [27] to generate more entanglement compared to the sudden switching function

$$\chi_\nu^{\text{sudden}}(t) = \begin{cases} 1 & \text{if } |t - t_\nu| < \frac{T}{2}, \\ 0 & \text{otherwise,} \end{cases} \tag{3.42}$$

due to the limited spectral content of the Gaussian function in the frequency space.

Let us now define some dimensionless quantities in relation to the switching timescale T:

$$\alpha_\nu = \Omega_\nu T, \tag{3.43}$$
$$\epsilon_\nu = \frac{x_\nu}{T}, \tag{3.44}$$
$$\epsilon = \epsilon_B - \epsilon_A = \frac{d}{T}, \tag{3.45}$$
$$\tau_\nu = \frac{t_\nu}{T}, \tag{3.46}$$
$$\gamma = \tau_B - \tau_A, \tag{3.47}$$
$$\delta = \frac{\sigma}{T}, \tag{3.48}$$
$$\kappa = kT, \tag{3.49}$$
$$\zeta = \frac{\beta}{T}. \tag{3.50}$$

We now calculate the integrals $\mathcal{L}$ and $\mathcal{M}$. First we define

$$L_\nu^{(s)}(\kappa) = \lambda \sqrt{\frac{1}{T}} \sqrt{\frac{|\kappa|}{2T}} C\left(\frac{\kappa}{T}\right) \widetilde{F}\left(\frac{\kappa}{T}\right) \cdot \sqrt{2\pi}\widetilde{\chi}_\nu\left(\frac{|\kappa| + s\alpha_\nu}{T}\right) \tag{3.51}$$

so that

$$\mathcal{L}_{\nu\eta}^{(s_A,s_B)} = \mathcal{L}_{\nu\eta,\,\text{vac}}^{(s_A,s_B)} + \int_{-\infty}^{\infty} \mathrm{d}\kappa \, \frac{e^{-i\kappa(\epsilon_\nu - \epsilon_\eta)}}{e^{\zeta|\kappa|} - 1} \left[(L_\nu^{(-s_\nu)}(\kappa))^* L_\eta^{(-s_\eta)}(\kappa) + L_\nu^{(s_\nu)}(\kappa) (L_\eta^{(s_\eta)}(\kappa))^* \right], \tag{3.52}$$

$$\mathcal{L}_{\nu\eta,\,\text{vac}}^{(s_A,s_B)} = \int_{-\infty}^{\infty} \mathrm{d}\kappa \, e^{-i\kappa(\epsilon_\nu - \epsilon_\eta)} L_\nu^{(s_\nu)}(\kappa) (L_\eta^{(s_\eta)}(\kappa))^*, \tag{3.53}$$

$$\mathcal{M}^{(s_A,s_B)} = \mathcal{M}_{\text{vac}}^{(s_A,s_B)} - \int_{-\infty}^{\infty} \mathrm{d}\kappa \, \frac{e^{-i\kappa\epsilon}}{e^{\zeta|\kappa|} - 1} \left[(L_A^{(-s_A)}(\kappa))^* L_B^{(s_B)}(\kappa) + L_A^{(s_A)}(\kappa) (L_B^{(-s_B)}(\kappa))^* \right]. \tag{3.54}$$

Now, the Fourier transform of the qubit smearing function is

$$\widetilde{F}\left(\frac{\kappa}{T}\right) = \frac{1}{\sqrt{2\pi}} e^{-\frac{1}{4}\kappa^2\delta^2}, \tag{3.55}$$

while the Fourier transform of the switching function is

$$\sqrt{2\pi}\widetilde{\chi}_\nu\left(\frac{|\kappa|+s\alpha_\nu}{T}\right) = \int_{-\infty}^{\infty} \mathrm{d}\tau\, T e^{-(\tau-\tau_\nu)^2} e^{i(|\kappa|+s\alpha_\nu)\tau} = \sqrt{\pi} T e^{-\frac{1}{4}(|\kappa|+s\alpha_\nu)^2} e^{i(|\kappa|+s\alpha_\nu)\tau_\nu}. \tag{3.56}$$

Thus equation (3.51) becomes

$$L_\nu^{(s)}(\kappa) = \lambda \frac{\sqrt{|\kappa|}}{2} C\left(\frac{\kappa}{T}\right) e^{-\frac{1}{4}\kappa^2\delta^2} e^{-\frac{1}{4}(|\kappa|+s\alpha_\nu)^2} e^{i(|\kappa|+s\alpha_\nu)\tau_\nu}. \tag{3.57}$$

Finally, we define

$$M^{(s_A,s_B)}(\kappa) = -\lambda^2 \frac{1}{T}\frac{|\kappa|}{2T} C_\xi^2\left(\frac{\kappa}{T}\right) \widetilde{F}^2\left(\frac{\kappa}{T}\right) e^{-i\kappa\epsilon} G^{(s_A,s_B)}(\kappa), \tag{3.58}$$

$$G^{(s_A,s_B)}(\kappa) = T^2 \int_{-\infty}^{\infty} \mathrm{d}\tau \int_{-\infty}^{\tau} \mathrm{d}\tau'\, e^{-i|\kappa|(\tau-\tau')} \left[e^{-(\tau-\tau_A)^2} e^{-(\tau'-\tau_B)^2} e^{i(s_A\alpha_A\tau + s_B\alpha_B\tau')} + (A \leftrightarrow B)\right] \tag{3.59}$$

such that

$$\mathcal{M}_{\text{vac}}^{(s_A,s_B)} = \int_{-\infty}^{\infty} \mathrm{d}\kappa\, M^{(s_A,s_B)}(\kappa). \tag{3.60}$$

Using the identity [27]

$$\int_{-\infty}^{\infty} \mathrm{d}\tau\, e^{-a^2 - ib\tau - \tau^2} \operatorname{erf}(\tau - ia) = -i\sqrt{\pi} e^{-a^2 - \frac{b^2}{4}} \operatorname{erfi}\left(\frac{a + \frac{b}{2}}{\sqrt{2}}\right) \tag{3.61}$$

we can integrate (3.59) to obtain

$$\begin{aligned} G^{(s_A,s_B)}(\kappa) = T^2 \frac{\pi}{2} e^{\frac{1}{4}\left(-\alpha_A^2 - \alpha_B^2 - 2\alpha_A\kappa - 2\kappa^2 - 4i\gamma k + 4i\tau_A(\alpha_A+\alpha_B) + 4i\alpha_B\gamma - 2(\alpha_A+\alpha_B+2i\gamma)|\kappa|\right)} \\ \cdot \Bigg\{ e^{\frac{1}{2}(\alpha_A+\alpha_B+2i\gamma)|\kappa|} \left(e^{\frac{1}{2}\alpha_B\kappa} + e^{\left(\alpha_A - \frac{\alpha_B}{2} + 2i\gamma\right)\kappa}\right) \\ + i e^{\frac{1}{2}(\alpha_A+2i\gamma)\kappa} \Bigg[e^{(\alpha_A+2i\gamma)|\kappa|} \operatorname{erfi}\left(\frac{\alpha_A - \alpha_B + 2i\gamma - 2|\kappa|}{2\sqrt{2}}\right) \\ - e^{\alpha_B|\kappa|} \operatorname{erfi}\left(\frac{\alpha_A - \alpha_B + 2i\gamma + 2|\kappa|}{2\sqrt{2}}\right) \Bigg] \Bigg\}. \end{aligned} \tag{3.62}$$

To finish the calculations, we let $\tau_A = 0$, $\tau_B = \gamma$, and we set $C_\xi(k) = [|k| \leq k_0]$, a sharp UV cutoff at k_0. We set

$$k_0 = 2\pi \cdot (50 \text{ GHz}) \tag{3.63}$$

as determined experimentally in [8], and the dimensionless quantity $\kappa_0 = k_0 T \approx 63$. Through numerics, we find that the integrands of the $\mathcal{L}_{\text{vac}}$ terms and parts of the $\mathcal{M}_{\text{vac}}$ contribute minimally for $|k| > k_0$, so that we may integrate them with no cutoff to find analytical expressions

$$\mathcal{L}^{(s_A,s_B)}_{\nu\nu,\,\text{vac}} = \lambda^2 \frac{e^{-\alpha_\nu^2/2}}{4(1+\delta^2)^{3/2}} \left[2\sqrt{1+\delta^2} - \sqrt{2\pi} s_\nu \alpha_\nu \exp\left(\frac{\alpha_\nu^2}{2(1+\delta^2)} \right) \operatorname{erfc}\left(\frac{s_\nu \alpha_\nu}{\sqrt{2(1+\delta^2)}} \right) \right], \tag{3.64}$$

$$\begin{aligned} \mathcal{L}^{(s_A,s_B)}_{AB,\,\text{vac}} &= \lambda^2 \frac{e^{-(\alpha_A^2+\alpha_B^2+4is_B\alpha_B\gamma)/4}}{8\sqrt{2}(1+\delta^2)^{3/2}} \\ &\quad \cdot \left[2D - \sqrt{\pi} A \exp\left(\frac{A^2}{D^2} \right) \operatorname{erfc}\left(\frac{A}{D} \right) - \sqrt{\pi} B \exp\left(\frac{B^2}{D^2} \right) \operatorname{erfc}\left(\frac{B}{D} \right) \right], \end{aligned} \tag{3.65}$$

$$\begin{aligned} \mathcal{M}^{(s_A,s_B)}_{\text{vac}} &= -\lambda^2 \frac{e^{-(\alpha_A^2+\alpha_B^2+4is_B\alpha_B\gamma)/4}}{8\sqrt{2}(1+\delta^2)^{3/2}} \\ &\quad \cdot \left[2D + \sqrt{\pi} A \exp\left(\frac{A^2}{D^2} \right) \operatorname{erfc}\left(\frac{A}{D} \right) + \sqrt{\pi} B \exp\left(\frac{B^2}{D^2} \right) \operatorname{erfc}\left(\frac{B}{D} \right) \right] \\ &\quad - \lambda^2 \frac{i}{4\sqrt{\pi}} \int_{-\kappa_0}^{\kappa_0} \mathrm{d}\kappa\, \kappa\, e^{\left(-\Sigma^2+4i\Sigma\gamma-4\gamma^2-8i\epsilon\kappa-4\delta^2\kappa^2\right)/8} \\ &\quad \cdot \left[D_+\left(\frac{\Sigma + 2i\gamma - 2\kappa}{2\sqrt{2}} \right) - D_+\left(\frac{\Sigma + 2i\gamma + 2\kappa}{2\sqrt{2}} \right) \right], \end{aligned} \tag{3.66}$$

where

$$A = \Sigma + 2i(\gamma - \epsilon), \quad B = \Sigma + 2i(\gamma + \epsilon), \quad D = 2\sqrt{2}\sqrt{1+\delta^2}, \quad \Sigma = s_A\alpha_A + s_B\alpha_B, \tag{3.67}$$

and

$$D_+(x) = e^{-x^2} \int_0^x \mathrm{d}t\, e^{t^2} \tag{3.68}$$

is the Dawson function.

Note that, in order to arrive at equation (3.66), where the absolute value $|\kappa|$ is dropped

in the integrand, we simply used the fact that for any $\kappa < 0$ and $z \in \mathbb{C}$,

$$|\kappa|\left[D_+\left(z - \frac{|\kappa|}{\sqrt{2}}\right) - D_+\left(z + \frac{|\kappa|}{\sqrt{2}}\right)\right] = -\kappa\left[D_+\left(z + \frac{\kappa}{\sqrt{2}}\right) - D_+\left(z - \frac{\kappa}{\sqrt{2}}\right)\right]$$
$$= \kappa\left[D_+\left(z - \frac{\kappa}{\sqrt{2}}\right) - D_+\left(z + \frac{\kappa}{\sqrt{2}}\right)\right].$$

We can integrate the thermal integrals in $\mathcal{L}_{\nu\eta}$, $\mathcal{M}$, and the remaining integral in (3.66), numerically, on the finite interval $\int_{-\kappa_0}^{\kappa_0} \mathrm{d}\kappa$.

The integral in (3.66) has a highly oscillatory integrand, which slows down the convergence of numerical integration. The integration performance can be improved by noting that the integrand is complex analytic, allowing us to integrate along the contour $[-\kappa_0, -\kappa_0 - 5i], [-\kappa_0 - 5i, \kappa_0 - 5i], [\kappa_0 - 5i, \kappa_0]$. By integrating along this contour, the oscillations are damped, and consequently the speed of convergence is improved.

3.3 Results

3.3.1 Parameters

To calculate the amount of entanglement possible with our current experimental setup, we set the following parameter values (note that some of them were set in the previous section in order to simplify calculations):

Table 3.1: Parameters chosen for the calculations of the entanglement harvesting experiment.

Parameter	Value
v	1.2×10^8 m/s
T	200 ps
λ	$1/4$
Ω_A, Ω_B	$2\pi\cdot$ (1.6–6.5 GHz)
α_A, α_B	$\Omega T \approx$ 2–8.1
τ_A	0
τ_B, γ	0
σ	$(24\,\mu\text{m})/v$
δ	$\sigma/T = 1/1000$
κ_0	$2\pi \cdot (50\text{ GHz}) \cdot T \approx 63$
T_{th}	20 mK
ζ	$1/(k_B T_{\text{th}} T) \approx 1.9$

In table 3.1, v is the speed of light in a typical superconducting coplanar waveguide as measured in [11]; T is chosen such that a fast arbitrary waveform generator (such as the Tektronix 70000A) can generate the required Gaussian pulse with minimal distortion; λ is chosen small enough such that the perturbative results are valid; Ω_A and Ω_B are chosen to in the operating range of the designed tunable qubits; σ is chosen as the approximate size of the qubit; and T_{th} is chosen as a feasible temperature for our dilution refrigerator. In the calculations that follow, we set the qubit gaps Ω_A and Ω_B to be the same: $\Omega_A = \Omega_B \equiv \Omega$, and $\alpha_A = \alpha_B \equiv \alpha$.

3.3.2 Initial States

Figure 3.2 shows the concurrence as a function of d and Ω for the four initial states $\hat{\rho}_{AB}^{(0)} \in \{|gg\rangle\langle gg|, |ee\rangle\langle ee|, |eg\rangle\langle eg|, |ge\rangle\langle ge|\}$. Here we have constrained $d \geq 5T$ in order to prevent a lightlike connection from forming between the two qubits: when $d \geq 5T$, we have $\chi_\nu(\pm d/2, t_\nu = 0) = e^{-(\pm d/2)^2/T^2} < 0.002$, which is smaller than one half of the resolution of the fast arbitrary waveform generators, implying that the switching is effectively turned off at $|t| = d/2$.

We can see that the only starting state that can generate non-negligible amounts of concurrence is $\hat{\rho}_{AB}^{(0)} = |eg\rangle\langle eg|$. Moreover, we can see that the concurrence is highly oscillatory in d, which could be a consequence of the finite UV cutoff. Lastly, we observe

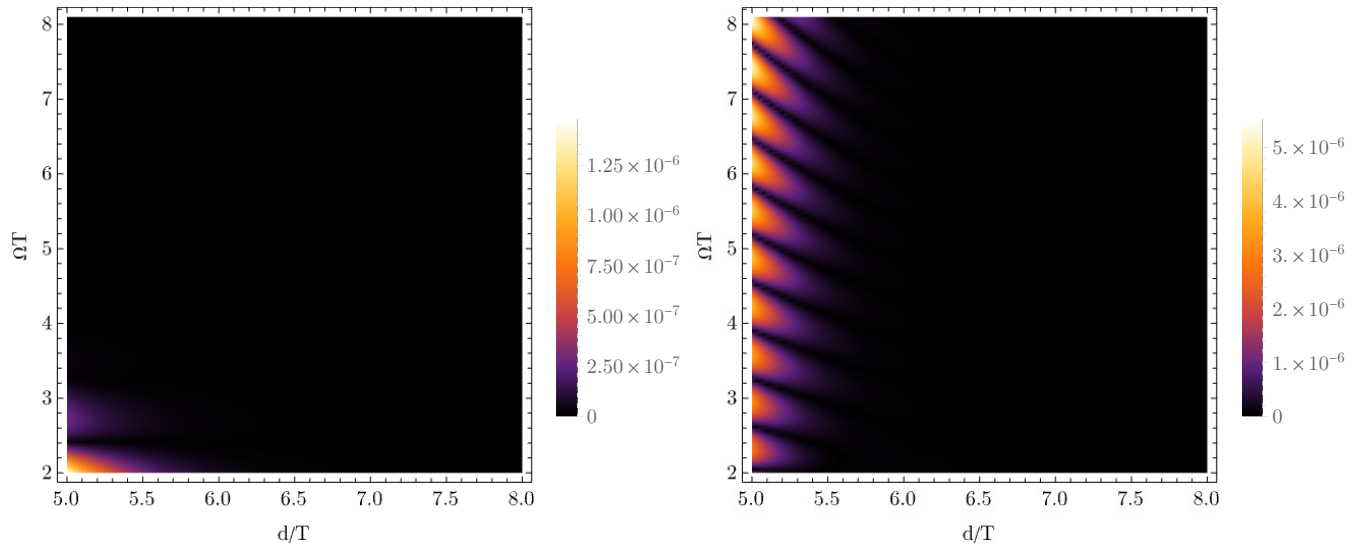

(a) $\hat{\rho}_{AB}^{(0)} = |gg\rangle\langle gg|$

(b) $\hat{\rho}_{AB}^{(0)} = |ee\rangle\langle ee|$

(c) $\hat{\rho}_{AB}^{(0)} = |eg\rangle\langle eg|$

(d) $\hat{\rho}_{AB}^{(0)} = |ge\rangle\langle ge|$

Figure 3.2: Concurrences as functions of d and Ω for different initial states, with $\lambda = 1/4$.

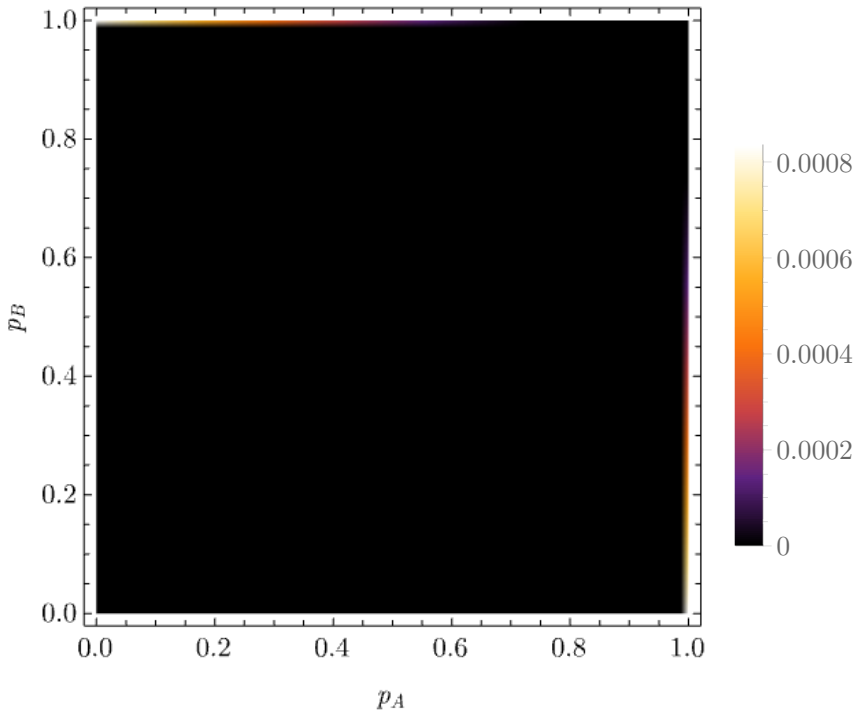

Figure 3.3: Concurrence with mixed initial state $\hat{\rho}_{AB}^{(0)} = (p_A \left|g_A\right\rangle\!\left\langle g_A\right| + (1-p_A) \left|e_A\right\rangle\!\left\langle e_A\right|) \otimes (p_B \left|g_B\right\rangle\!\left\langle g_B\right| + (1-p_B) \left|e_B\right\rangle\!\left\langle e_B\right|)$, with $\lambda = 1/10$, $\alpha = 8.08$, $\epsilon = 5.111$.

that a higher energy gap Ω is required as we increase d in order to get a nonzero concurrence. Since d is fixed in a real experiment, we can in theory observe the oscillatory behaviour by varying T, the timescale of the Gaussian switching function.

Figure 3.3 shows the amount of entanglement we can harvest at the optimal point starting with a mixed state, and with $\alpha = 8.08$ and $\epsilon = 5.111$. Here we set $\lambda = 0.1$, since otherwise some density matrix elements become negative depending on the value of p_A and p_B. We can see that only when one of pA, pB is very nearly 1 while the other is much greater than 0 will we observe a nonzero concurrence. Thus, it is important to ensure that the qubits are prepared in mostly pure states. For a two-level qubit with gap Ω at temperature T_{th}, the thermal equilibrium state of the qubit is the Gibbs state

$$\hat{\rho}^{(0)}_{T_{\text{th}}} = \frac{e^{-\hat{H}/(k_B T_{\text{th}})}}{\text{Tr}[e^{-H/(k_B T_{\text{th}})}]} = \frac{1}{1 + e^{-\Omega/(k_B T_{\text{th}})}} \left(|g\rangle\langle g| + e^{-\Omega/(k_B T_{\text{th}})} |e\rangle\langle e| \right). \tag{3.69}$$

Plugging in the parameters for our qubit, $\Omega = 2\pi \cdot 6.5$ GHz, $T_{\text{th}} = 20$ mK, we find that its relaxed state is approximately

$$\hat{\rho}^{(0)}_{T_{\text{th}}} = (1 - 5 \times 10^{-7}) |g\rangle\langle g| + (5 \times 10^{-7}) |e\rangle\langle e| . \tag{3.70}$$

This state is effectively in the ground state with negligible impurity.

Finally, note that at the optimal point, the distance between the two qubits is $\epsilon T c \approx 12$ cm on the transmission line. This can be easily done with a meandering coplanar waveguide on the device.

3.3.3 Transmission Line Temperature

Figure 3.4 shows the concurrence as a function of the transmission line temperature T_{th}, with initial state $\hat{\rho}^{(0)}_{AB} = |eg\rangle\langle eg|$, at the point of maximal concurrence from the previous section. As expected, as we increase the qubit temperature, the amount of entanglement we can harvest decreases. For the parameters we are considering, a hard cutoff happens at around $T_{\text{th}} = 30$ mK. Thus, it is very important to ensure that the sample device stays below this limit during an experiment.

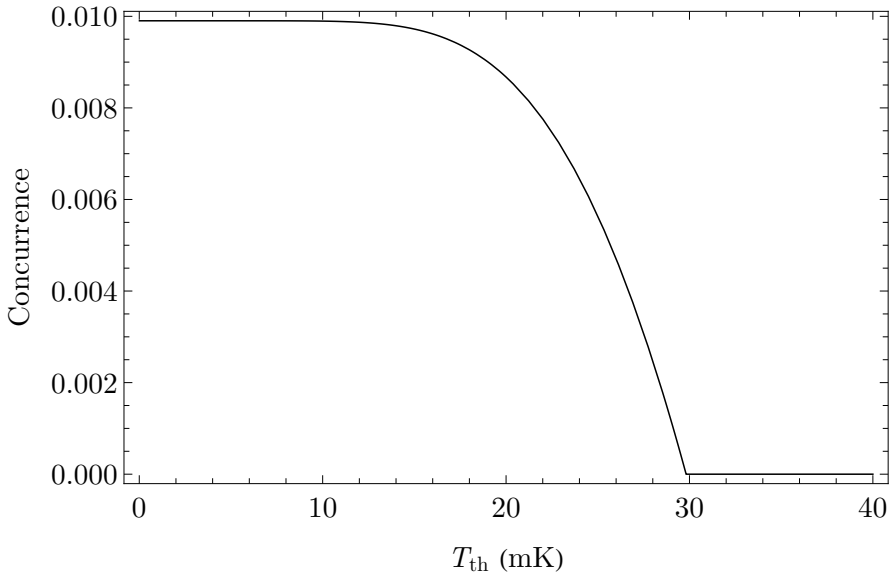

Figure 3.4: Concurrence as a function of the transmission line temperature T_{th}, with $\hat{\rho}_{AB}^{(0)} = |eg\rangle\langle eg|$, $\alpha = 8.08$, $\epsilon = 5.111$.

3.3.4 Density Matrix

The density matrix $\hat{\rho}_{AB}$ at the optimal point, where $\lambda = 1/4$, $\sigma = 1/1000$, $\epsilon = 5.111$, $T_{\text{th}} = 20$ mK, and $\alpha = 8.08$, is approximately

$$\hat{\rho}_{AB} = \begin{pmatrix} 0.63 & 0 & 0 & -2.5 \times 10^{-20} \\ 0 & 0.37 & 4.2 \times 10^{-7} - 0.0050i & 0 \\ 0 & 4.2 \times 10^{-7} + 0.0050i & 0 & 0 \\ -2.5 \times 10^{-20} & 0 & 0 & 6.0 \times 10^{-7} \end{pmatrix}. \tag{3.71}$$

The main contribution to the concurrence of this density matrix is its $|\rho_{23}|$ term. We can see that the magnitude of this term is very small, around 5×10^{-3}. To successfully detect entanglement in this case, we need to use a robust qubit readout and state tomography procedure during an experimental run.

Finally, we would like to note that, from the results of nonperturbative calculations for harvesting entanglement with simpler switching functions in [30], we can reasonably expect the concurrence to be proportional to λ^2 to the order of $\lambda \sim 1$. Relating λ to the spin-boson coupling strength α_{SB}, by using the relation [22]

$$\lambda = \sqrt{2\pi\alpha_{\text{SB}}}, \tag{3.72}$$

we can see that this corresponds to an α_{SB} of around 0.16, which is well within the ultrastrong coupling regime obtainable by the designed device in section 4.1. Extrapolating from the concurrence we got for $\lambda = 0.25$, which is approximately 0.0087, we can expect the concurrence to increase to $0.0087 \cdot (1/0.25)^2 \approx 0.14$. This would be much easier to detect in an experimental setting.

3.4 Conclusions

In this chapter, we derived the coupling model of a flux qubit coupled to a transmission line, then we applied perturbation theory to calculate the amount of entanglement that we can harvest with a realistic setup, for different starting conditions. We found that to produce a non-negligible amount of entanglement when the coupling of the qubits are spacelike separated, we need to initialize the qubits to $|eg\rangle\langle eg|$ or $|ge\rangle\langle ge|$; and that the temperature of the device should be kept at around 20 mK or less. Finally, we discussed the difficulties in performing quantum state tomography on the calculated final states. While challenging, with current experimental equipment, it is hopeful that the phenomenon of entanglement harvesting can be observed.

Chapter 4

Implementation of the Entanglement Harvesting Experiment

Using the parameters found in chapter 3, we can devise an experiment design that enables the demonstration of the phenomenon of entanglement harvesting. In this chapter, we propose such a design and perform simulations to validate the feasibility of our design.

This chapter is organized as follows. In section 4.1, we present and discuss the design of the device that will allow us to perform the experiment. In section 4.2, we propose the main experimental protocol for entanglement harvesting with our device. Finally, in section 4.3, we propose a state tomography procedure that allows us to detect the entanglement harvested from the main experimental protocol.

4.1 Device Design

In this section, we present the design of the device that we will use for the entanglement harvesting experiment.

4.1.1 Qubit With a Tunable Coupler From Weak to Ultrastrong Coupling

To implement the entanglement harvesting experiment, we need a qubit that has tunable coupling to a transmission line with a range that can cover full decoupling to the ultrastrong

coupling regime. Such a qubit was recently designed to fulfill this role [29]. We call this design the USC qubit in short.

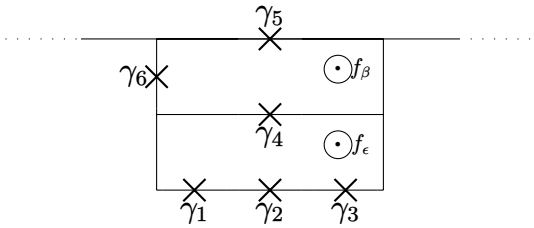

Figure 4.1: Circuit model of the USC qubit. Here, the qubit shares junction 5 with transmission line. The botoom loop is the main qubit loop, or the ϵ loop, while the top loop is the coupler loop, or the β loop.

Figure 4.1 shows the schematic of the USC qubit. It consists of a four loop persistent current flux qubit and a coupler galvanically coupled together to a transmission line. The coupler design is based on a SQUID, that is inductively coupled to the main qubit and to the transmission line. We will call the main qubit as the ϵ loop, while we will call the coupler qubit the β loop.

Because of the inclusion of a SQUID-based coupler, this design allows the dynamic switching of the main qubit's coupling to the transmission line from full decoupling to the non-perturbative USC regime and beyond. The coupling of the qubit to the transmission line is tuned by varying the external magnetic frustration f_β of the β qubit.

We can simulate the properties of this qubit design numerically. Following standard procedures, we can write down the Hamiltonian of the qubit as [29]

$$\hat{H} = \frac{1}{2\varphi_0^2}\hat{\mathbf{p}}^\mathsf{T} C^{-1}\hat{\mathbf{p}} + \hat{U}. \tag{4.1}$$

Here we defined

$$\hat{\mathbf{p}} = \begin{pmatrix} \hat{p}_1 \\ \hat{p}_2 \\ \hat{p}_4 \\ \hat{p}_5 \end{pmatrix}, \tag{4.2}$$

with $\hat{p}_i = \varphi_0^2 \sum_j C_{ij}\hat{\gamma}_j$ being the momentum conjugate to the variable γ_i,

$$C = \begin{pmatrix} C_1 + C_3 & C_3 & C_3 & 0 \\ C_3 & C_2 + C_3 & C_3 & 0 \\ C_3 & C_3 & C_3 + C_4 + C_6 & C_6 \\ 0 & 0 & C_6 & C_5 + C_6 \end{pmatrix} \tag{4.3}$$

is the capacitance matrix of the system, with C_i being the capacitance of junction i; and

$$\begin{aligned}\hat{U} = -\varphi_0\Big[&I_{C1}\cos\hat{\gamma}_1 + I_{C2}\cos\hat{\gamma}_2 + I_{C3}\cos(\hat{\gamma}_1+\hat{\gamma}_2+\hat{\gamma}_4+2\pi f_\epsilon)\\ &+ I_{C4}\cos\hat{\gamma}_4 + I_{C5}\cos\hat{\gamma}_5 + I_{C6}\cos(\hat{\gamma}_4+\hat{\gamma}_5-2\pi f_\beta)\Big]\end{aligned} \tag{4.4}$$

is the potential energy of the system.

For convenience, we work with the charge basis $\{|n_1\rangle\cdots|n_6\rangle : n_i \in \mathbb{Z}\}$. In this basis, we have

$$\hat{p}_i = \hbar\hat{n}_i, \tag{4.5}$$

$$\cos\hat{\gamma}_i = \frac{e^{i\hat{\gamma}_i}+e^{-i\hat{\gamma}_i}}{2}|n_i\rangle = \frac{|n_i+1\rangle+|n_i-1\rangle}{2}. \tag{4.6}$$

We can write the Hamiltonian as a matrix in the charge basis by writing each $\hat{n}_i$ in its diagonal form, truncated to $[-n_{i,\max}, n_{i,\max}]$:

$$\hat{n}_i = \begin{pmatrix} -n_{i,\max} & & & \\ & -n_{i,\max}+1 & & \\ & & \ddots & \\ & & & n_{i,\max} \end{pmatrix}. \tag{4.7}$$

With the Hamiltonian in its matrix form, we can use standard numerical diagonalization techniques in order to determine its eigenstates and eigenvalues, and thus determine the qubit transition frequency E_{01}, the anharmonicity E_{12}/E_{01}, and its two lowest states $|0\rangle$ and $|1\rangle$.

To estimate the relaxation rate Γ_1 and the pure dephasing rate Γ_φ, we use the approximations [29]

$$\Gamma_1 = \frac{\Delta^2 R_Q}{2\pi E_{01} Z_0}|\langle 1|\hat{\gamma}_\beta|0\rangle|^2, \tag{4.8}$$

and

$$\Gamma_\varphi = \frac{E_{01}^2-\Delta^2}{2E_{01}^2}|\langle 0|\hat{\gamma}_\beta|0\rangle - \langle 1|\hat{\gamma}_\beta|1\rangle|^2\frac{R_Q k_B T}{Z_0 h}. \tag{4.9}$$

Here, $R_Q = h/(2e)^2 \approx 6.5\ \mathrm{k\Omega}$ is the quantum resistance, $Z_0 = 50\ \Omega$ is the impedance of the transmission line, Δ is the qubit energy gap at the symmetry point, and

$$\langle n|\hat{\gamma}_\beta|m\rangle = \frac{1}{2\pi}\int_{-\pi}^{\pi} \mathrm{d}\gamma_\beta\, \gamma_\beta e^{-i(m-n)\gamma_\beta} = \begin{cases} 0 & \text{if } m=n, \\ i(-1)^{m-n+1}/(m-n) & \text{otherwise,} \end{cases} \tag{4.10}$$

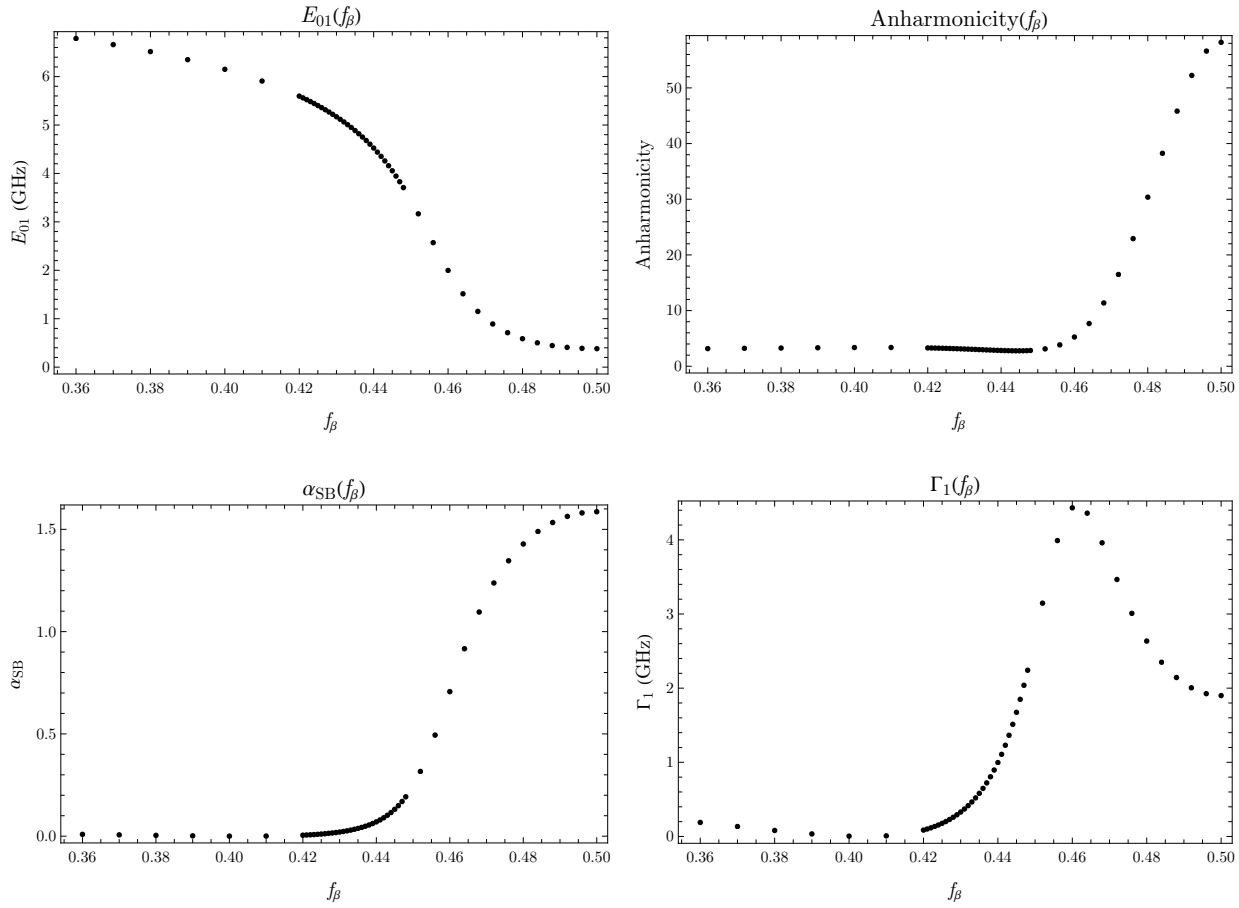

Figure 4.2: The simulated properties of the USC qubit at its symmetry point, as functions of f_β. (a) The qubit gap E_{01}. (b) The anharmonicity E_{12}/E_{01}. (c) The spin-boson coupling strength α_{SB}. (d) The relaxation rate Γ_1.

are the matrix elements of $\hat{\gamma}_\beta$.

For the simulations, we have set $n_{1,\max} = n_{2,\max} = 5$, $n_{4,\max} = n_{5,\max} = 7$, and we use the qubit design parameters given in table 4.1.

Table 4.1: Optimized USC qubit parameters.

Parameter	Description	Value
$A_{1/3}$	Size of junction 1/3	0.079 μm^2
r_2	Area ratio of junction 2 to junction 1	0.58
$r_{4/5}$	Area ratio of junction 4/5 to junction 1	1.78
r_6	Area ratio of junction 6 to junction 1	0.92
J_c	Junction critical current density	3 μA/μm^2

These parameters are found by optimizing the USC qubit for desirable properties such as a reasonable qubit gap, a relatively long relaxation time, and the ability to couple ultrastrongly to the transmission line [29]. More specifically, we require the qubit gap to be in the range of 1–12 GHz to stay within the bandwidth of our microwave setup. Moreover, we require the relaxation time T_1 to be much larger than the time for state preparation, which is in the order of 10 ns. Lastly, we require the spin-boson coupling strength α_{SB} to be tunable from 0 to 1+.

The simulation results are plotted in 4.2, where we plotted the qubit gap E_{01}, the anharmonicity E_{12}/E_{01}, the spin-boson coupling factor α_{SB}, and the relaxation rate Γ_1, as functions of the β flux f_β. Because we always operate the flux qubit at its symmetry point except for when we do readout, the values are generated at the symmetry points. To stay at symmetry point, when we adjust f_β, we need to tune f_ϵ as well. For every f_β, we can find the f_ϵ value at the symmetry point by minimizing the qubit gap with respect to f_ϵ. The symmetry point fluxes are plotted in figure 4.3.

From the plots, we can see that the USC qubit can easily be tuned to have an α_{SB} from 0 to more than 1.5, thus allowing tunable coupling into the non-perturbative ultrastrong coupling regime. The decoupling point occurs near $f_\beta = 0.4$, with a Γ_1 of around 4 MHz, or a T_1 of 400 ns. The relaxation time is much greater than the time required to perform operations on the qubit, such as state preparation and readout prerotation, which takes around 10 ns. For the energy gap E_{01}, we can see that it is around 6 GHz at the decoupling point, and dips to below 3 GHz when it enters the USC regime. This is fully within the range of our current microwave setup.

Finally, we need to find a suitable readout point. At the readout point, the qubit should be decoupled from the transmission line, and biased far away from the symmetry point. This

way, the qubit will be in the flux state, and we can readout its state via inductive coupling to a DC-SQUID readout circuit. To bias the qubit away from its symmetry point, we can simply increase the flux f_ϵ, while keeping f_β constant. The flux configuration $f_\beta = 0.4$, $f_\epsilon = 0.445$ is a good candidate—at this point, the relaxation time is around $T_1 \approx 2.5\,\mu$s, providing ample time for readout.

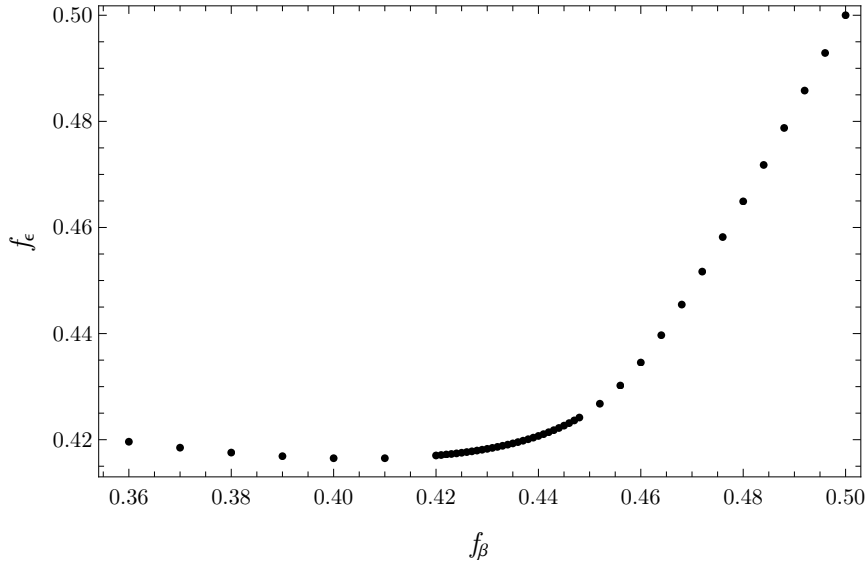

Figure 4.3: Flux values at the symmetry point of the USC qubit.

4.1.2 RQI Device

The sample device for the entanglement experiment, which we call the RQI (relativistic quantum information) device, is essentially a device that has two USC qubits coupled to the same transmission line separated far apart. From section 3.3.2, we estimated that the optimal separation between the two qubits is around 12 cm. Because the sample holder can only hold sample devices that has a maximum of dimension of around 1 cm $\times$ 1 cm, we need to meander the on-chip transmission line to increase the separation between the two qubits to 12 cm.

The chip layout of the RQI device is given in figure 4.4. Here we can see that there are two USC qubits at the left and the right side of device, which are galvanically coupled to a long meandering transmission line with the length between the qubits being around 12 cm. Each qubit has two flux control lines, coupled to the β and ϵ loops respectively.

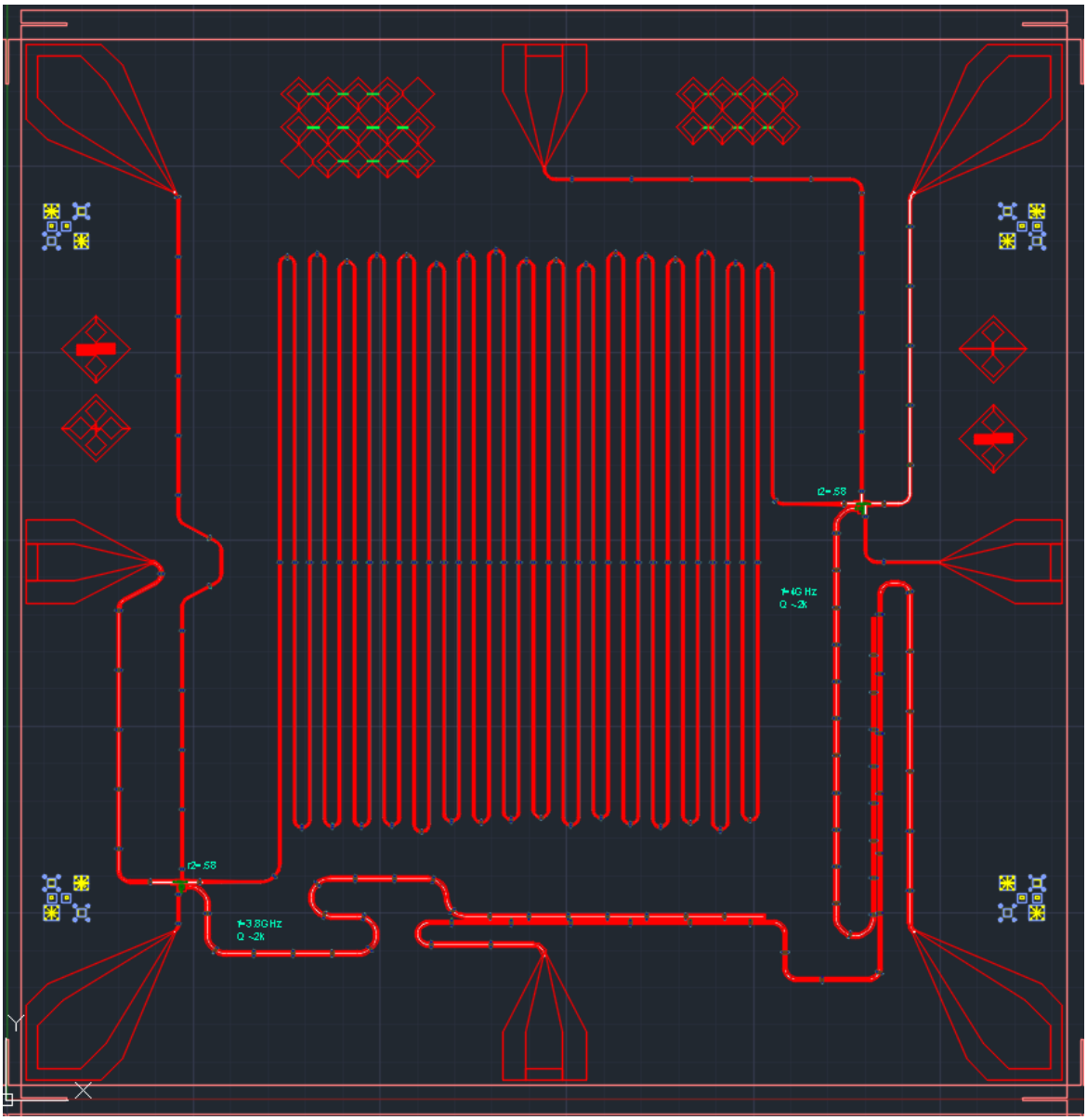

Figure 4.4: Chip layout of the RQI device. Two USC qubits are coupled to a long meandering transmission line. The readout circuit consists of DC-SQUIDs coupled to readout resonators. The dimensions of the device are 7×7 mm.

As discussed in section 3.3.2, we chose 12 cm as the distance between the qubits, so that using a Gaussian switching function with a characteristic time $T \approx 200$ ps, a lightlike connection between the qubits will not form. We varied the lengths of the straight sections the transmission line to mitigate unwanted coupling between sections. Finally, we simulated the meandering transmission line design in Sonnet, and we confirmed that this transmission line has good loss and reflection characteristics from DC to 50 GHz.

The readout circuit for a single qubit consists of a DC-SQUID near the qubit, capacitively coupled to a superconducting microwave resonator with a resonance frequency of around 4 GHz, which is then coupled inductively to a readout feedline. The feedline is a coplanar waveguide that is has its ends connected to the readout microwave electronics outside the device. The readout resonators of the two qubits are then coupled to the same feedline. This allows multiplexed readout, which greatly simplifies the readout electronics.

The RQI device is fabricated using a planar process involving four layers, on top of a silicon substrate, with aluminum being the superconductor. Optical and electron beam lithography are used to pattern the features of this device. Moreover, we add superconducting air bridges that bridges the ground planes divided by the coplanar waveguides, to improve the uniformity of the ground plane and to reduce the decoherence rate of the qubit. To make the Josephson junctions, we use a standard fabrication technique where aluminum is first evaporated at a slanted angle, then the deposited aluminum is oxidized, and finally aluminum is evaporated at another angle [7].

4.2 Experimental Protocol

In this section, we describe the protocol for the entanglement harvesting experiment in detail. The experiment at the high level is described in chapter 3. To summarize, the idea is that we need to prepare the two USC qubits on the RQI device into states $|e\rangle$ and $|g\rangle$ respectively, while they are decoupled from the transmission line. Then, we couple the qubits strongly to the transmission line for a short amount of time (< 1 ns), using a Gaussian switching function. Finally, after the qubits are decoupled from the transmission line, we perform quantum state tomography on the qubits. With enough repetitions, we can reconstruct the density matrix of the two qubit system and thus calculate its concurrence.

More specifically, we perform the experiment in the following steps:

1. Set the two qubits at their decoupling points. This can be done by biasing the fluxes f_β and f_ϵ to the appropriate values found in simulation and calibration.

2. Prepare the two qubits into the excited $|e\rangle$ and ground $|g\rangle$ states respectively. This can be done by first allowing the qubits to relax to their thermal equilibrium states, then exciting the first qubit.

   From equation (3.70), by simply allowing the qubits to relax to their thermal equilibrium state, we can prepare the qubits to $|g\rangle$ with high fidelity. Furthermore, from the simulations of the USC qubit, at the decoupling point, the relaxation rate Γ_1 is around 4 MHz. Hence, if we wait for around 10 μs after each run, the qubits will have relaxed to their ground states with high fidelity regardless of their initial state.

   In order to excite the first qubit into its excited state, we can apply a π Rabi pulse around the x-axis to the first qubit. Because the USC qubit has a Rabi frequency in the order of 1 GHz [29], the pulse only needs to be a few nanoseconds in duration.

3. Couple the qubits to the transmission line with the coupling strength governed by the time-dependent switching function.

   We need to vary the coupling strength α_{SB} of the two qubits simultaneously according to the equation

   $$\alpha_{\text{SB}}(t) = \frac{\lambda^2}{2\pi}\chi^2(t). \tag{4.11}$$

   Using the Gaussian switching function (3.41), we obtain

   $$\alpha_{\text{SB}}(t) = \frac{\lambda^2}{2\pi}e^{-2t^2/T^2}. \tag{4.12}$$

   Since the Gaussian switching function $\chi(t)$ is suppressed to a negligible amount for $|t| > 2.5T$, we can start this stage at around $t \approx -2.5T$ and finish at around $t \approx 2.5T$.

   From section 4.1.1, we can map an α_{SB} to a flux pair (f_β, f_ϵ) that is at the qubit's symmetry point. We can thus vary the fluxes f_β and f_ϵ according to this data in order to get the desired α_{SB}.

After we have coupled and decoupled the qubits, we can proceed with quantum state tomography on the qubits. This procedure is described in detail in section 4.3.

4.3 Quantum State Tomography

Quantum state tomography (QST) is a procedure to reconstruct the density matrix of a quantum state through repeated measurements done on identical quantum states. For this

experiment, we will use a popular technique called maximum likelihood estimation, or MLE in short. In essence, MLE reconstructs the density matrix of a system by first collecting population data of the system in different bases, then find the density matrix that is most likely to generate the measured population data [16]. In this section, we outline the protocol for QST that is specific for our setup, using the MLE method.

The data collection procedure for QST is as follows:

1. Apply a prerotation operation on the qubits.

   The experimental setup is limited to performing readout in the standard Z basis. Thus, in order to collect statistics of the populations in other bases, we need to rotate the qubits from the desired bases to the Z basis.

   For our two qubit setup, we can apply one of the nine prerotations in

   $$P = \{I, R_x(\pi/2), R_y(\pi/2)\} \otimes \{I, R_x(\pi/2), R_y(\pi/2)\}. \tag{4.13}$$

   The x pulses can be calibrated by scaling the pulse times by the experimentally measured Rabi time at a certain amplitude. For y pulses, we can use the same parameters as their x counterparts, but with the phase shifted by $\pi/2$.

2. Perform readout on the qubits in the standard Z basis.

   This can be done by first biasing the qubits far away from their symmetry points in an adiabatic manner, so that the qubits will settle into their flux bases while maintaining their states. Afterwards, we send a microwave pulse through each of the feedline coupled to the readout circuits of the qubits. Depending on whether the qubit is in its ground or excited state, the resonant frequency of the resonator will be shifted. This shift can be detected by a drop in the signal level of the resonator's response to the microwave pulse, which can be measured using a data acquisition card after a suitable amount of low-noise amplification is applied.

   We can perform readout on the two qubits at once. Since the readout resonators are designed to have a resonant gap of around 100 MHz, we can send a multiplexed signal through the feedline that has a tone at the resonators' resonant frequencies, ω_1 and ω_2, and perform heterodyne readout on the collected voltage data.

   In detail, the readout is done as follows. First, we send a multiplexed readout signal through the readout line. Let $\omega_{LO} = (\omega_A + \omega_B)/2$ and $\Omega_{IF} = \omega_B - \omega_{LO} = \omega_{LO} - \omega_A$. We use an IQ mixer with its LO frequency set to ω_{LO} and generate the multiplexed intermediate signal at frequencies $\pm\omega_{IF}$. The IQ mixer will upconvert the intermediate

signal to $\omega_{LO} \pm \omega_{IF}$, which we can then send to the feedline. The response signal coming out of the readout line is then downconverted using another IQ mixer in phase with the upconverting mixer. This signal is then acquired by the data acquisition card, at a sampling rate of 200 MHz or more, into a discrete complex voltage array $V[t_i]$. The real and imaginary components of the array contains the I and Q signals coming out of the IQ mixer.

We can then detect the state of the qubits by checking the signal level at $\pm\omega_{IF}$. If there is a signal at $+\omega_{IF}$ ($-\omega_{IF}$), then qubit A(B) is in the ground state. Otherwise, the qubit is in the excited state. To obtain the signal level at $\pm\omega_{IF}$, we apply a single-bin DFT:

$$V_{\pm\omega_{IF}} = \mathrm{Re}\left\{\frac{2}{n}\sum_{i=1}^{n} V[t_i]e^{-i2\pi(\pm\omega_{IF})t_i}\right\}. \tag{4.14}$$

For clarity, we write $V_A = V_{-\omega_{IF}}$, and $V_B = V_{\omega_{IF}}$, where the subscript index represents the qubit index. We can scale the signals by the ground and excited signals for each qubit into scaled signals denoted by Z_A and Z_B. We scale the voltage signals such that for a perfect signal, $Z_n = 1$ if qubit n is in its ground state, and -1 otherwise.

After each run, we save Z_A, Z_B, and in addition $Z_A Z_B$. The last term is required to reconstruct the off-diagonal terms in the density matrix, necessary for the detection of entanglement.

To reduce noise and obtain statistics on the qubit population, we can repeat steps 1 and 2 many times to obtain three average voltage levels for each qubit and prerotation. we denote the averages by $\langle Z_A I_B\rangle_{\hat{U}}$, $\langle I_A Z_B\rangle_{\hat{U}}$, and $\langle Z_A Z_B\rangle_{\hat{U}}$, where $\hat{U} \in P$ is the prerotation operator applied.

We can now apply the MLE method to reconstruct the density matrix $\hat{\rho}$. Define the measurement operator for each qubit in the Z basis as

$$\hat{Z}_{A/B} = \left|g_{A/B}\right\rangle\!\left\langle g_{A/B}\right| - \left|e_{A/B}\right\rangle\!\left\langle e_{A/B}\right|, \tag{4.15}$$

Given a density matrix $\hat{\rho}$ and a measurement operator $\hat{M}$, the expected ensemble average of performing this measurement is $\mathrm{Tr}[\hat{M}\hat{\rho}]$. The MLE method essentially finds a density matrix that minimizes the difference between $\mathrm{Tr}[\hat{M}\hat{\rho}]$ and the measured value [16].

More specifically, we solve the following semidefinite program

$$\min_{\hat{\rho}} \sum_{\substack{\hat{U}\in P,\\ M\in\{Z_A I_B, I_A Z_B, Z_A Z_B\}}} \left(\mathrm{Tr}\left[\hat{M}\hat{U}\hat{\rho}\hat{U}^\dagger\right] - \langle M\rangle_{\hat{U}}\right)^2 \quad \text{subject to} \quad \hat{\rho} \geq 0, \mathrm{Tr}\,\hat{\rho} = 1, \tag{4.16}$$

where $\hat{\rho}$ is a 4×4 Hermitian matrix. This program can be easily solved with a convex optimization software such as MOSEK [2].

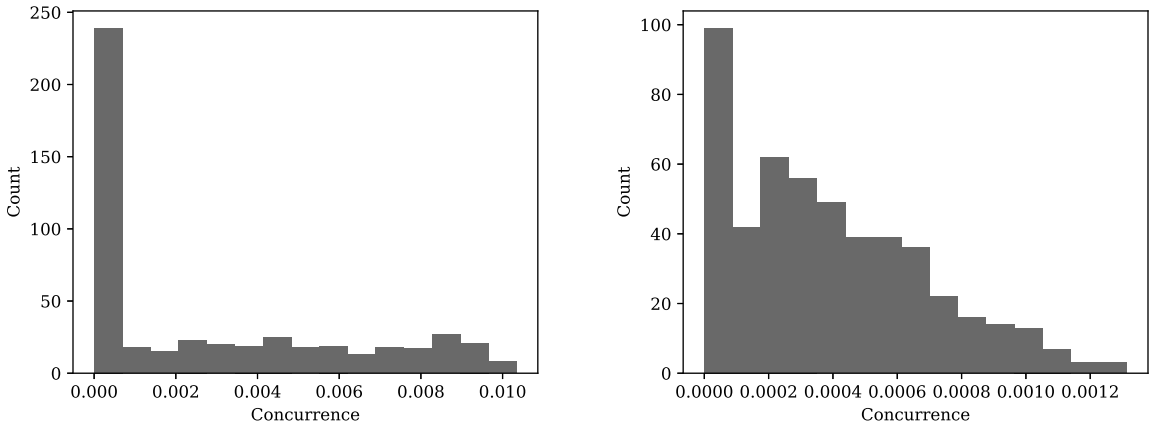

(a) $\hat{\rho} =$ (3.71)

(b) $\hat{\rho} = |eg\rangle\langle eg|$

Figure 4.5: Concurrences of reconstructed density matrices from simulated noisy QST. The target density matrix is (a) the density matrix at the optimal point given in (3.71), and (b) $|eg\rangle\langle eg|$.

We simulated the QST procedure given above with different density matrices, to determine the robustness of the procedure in the presence of noise. For a given target $\hat{\rho}$, the simulation generates the measurement data by generating first the scaled signals ± 1 randomly with the probability of the signal being 1 being $\mathrm{Tr}[|e\rangle\langle e| \hat{U}\hat{\rho}\hat{U}^\dagger]$. After the signals are generated, we add random Gaussian noise to each sample. The Gaussian has a standard deviation of $\sigma = 1$, chosen such that a one-shot single qubit measurement with a simple discriminator has fidelity of around 80%, which is roughly in line with our setup. We generate 10^7 noisy signals for each prerotation operator. After the signals are generated, we apply the MLE procedure to recover the density matrix, and we calculate its concurrence. Finally, we repeat this simulation 500 times for each target $\hat{\rho}$ in order to generate the statistics of the reconstructed concurrences.

The simulation results are plotted in 4.5. Here we plotted the histogram of reconstructed concurrences from running the QST procedure 500 times on $\hat{\rho} =$ (3.71), the density matrix at the optimal point found in chapter 3, and on $\hat{\rho} = |eg\rangle\langle eg|$, a separable state. In figure 4.5a, nearly half of its reconstructed concurrences are zero, while the other half are spread evenly across a concurrence range from 0.001 to 0.01. Compared to figure 4.5b, we can

see that there is a much larger spread of concurrence values. By repeating QST many times and detecting when a high amount of concurrence is generated, we can effectively distinguish (3.71) from $|eg\rangle\langle eg|$ and other separable states.

If we set the repetition t_{rep} to 15 μs, we can complete a QST run in $10^7 \cdot 9 \cdot 15\mu\text{s} = 22.5$ minutes. This amount of time to collect a single datum is reasonable for an experiment.

4.4 Summary

In this chapter, we presented the design of the RQI device to be used for the experiment, and we outlined an experimental protocol that can be implemented realistically to demonstrate the harvesting of entanglement. Thorough numerical simulation, we validated that our protocol can indeed detect the harvested entanglement with reasonable conditions.

Chapter 5

Conclusions

This thesis presented an analysis of the conditions of feasibility of performing the entanglement harvesting experiment with a superconducting flux qubit, and outlined the protocol for performing the experiment.

In chapter 2, we introduced the theoretical building blocks of the proposed entanglement harvesting experiment. More specifically, we introduced the superconducting flux qubit, the control and readout methods of the qubit, the quantization of the transmission line, and the Unruh-DeWitt detector. Together, they allowed us to analyze and propose an implementation of the entanglement harvesting experiment using superconducting flux qubits in chapters 3 and 4.

In chapter 3, we derived the expressions of the amount of entanglement that can be harvested using a flux qubit tunably coupled to an open transmission line. We then calculated the amount of entanglement possible with a range of realistic experimental parameters. We found that, under the right conditions, we can generate a non-negligible amount of entanglement that can be detected experimentally.

In chapter 4, we outlined the design and the protocol of the RQI device that will be used for the entanglement harvesting experiment. We validated our protocol through simulations, and found that it can be used to detect the generated entanglement from entanglement harvesting in a real experiment with noise in measured data.

In summary, we have outlined, in this thesis, the necessary conditions for the harvesting of entanglement to be observable, and an experiment design to demonstrate this phenomenon, that can be implemented with current technology. Future work involves constructing the microwave hardware necessary to implement the proposed protocol, and performing the experiment with the proposed protocol on a physical RQI device.

References

[1] Vinay Ambegaokar and Alexis Baratoff. Tunneling between superconductors. *Phys. Rev. Lett.*, 10:486–489, Jun 1963.

[2] MOSEK ApS. *MOSEK Fusion API for Python 9.3.18*, 2022.

[3] J. Bardeen, L. N. Cooper, and J. R. Schrieffer. Microscopic theory of superconductivity. *Phys. Rev.*, 106:162–164, Apr 1957.

[4] Alexandre Blais, Arne L. Grimsmo, S. M. Girvin, and Andreas Wallraff. Circuit quantum electrodynamics. *Rev. Mod. Phys.*, 93:025005, May 2021.

[5] Eric G Brown, William Donnelly, Achim Kempf, Robert B Mann, Eduardo Martín-Martínez, and Nicolas C Menicucci. Quantum seismology. *New Journal of Physics*, 16(10):105020, oct 2014.

[6] Claude Cohen-Tannoudji, Bernard Diu, and Franck Laloë. *Quantum Mechanics*. Wiley, 2005.

[7] G. J. Dolan. Offset masks for lift-off photoprocessing. *Applied Physics Letters*, 31(5):337–339, 1977.

[8] P. Forn-Díaz, J. J. García-Ripoll, B. Peropadre, J. L. Orgiazzi, M. A. Yurtalan, R. Belyansky, C. M. Wilson, and A. Lupaşcu. Ultrastrong coupling of a single artificial atom to an electromagnetic continuum in the nonperturbative regime. *Nature Physics*, 13(1):39–43, 2017.

[9] Javier Galego, Francisco J. Garcia-Vidal, and Johannes Feist. Cavity-induced modifications of molecular structure in the strong-coupling regime. *Phys. Rev. X*, 5:041022, Nov 2015.

[10] Salvatore Gambino, Marco Mazzeo, Armando Genco, Omar Di Stefano, Salvatore Savasta, Salvatore Patanè, Dario Ballarini, Federica Mangione, Giovanni Lerario, Daniele Sanvitto, and Giuseppe Gigli. Exploring light–matter interaction phenomena under ultrastrong coupling regime. *ACS Photonics*, 1(10):1042–1048, 10 2014.

[11] M. Göppl, A. Fragner, M. Baur, R. Bianchetti, S. Filipp, J. M. Fink, P. J. Leek, G. Puebla, L. Steffen, and A. Wallraff. Coplanar waveguide resonators for circuit quantum electrodynamics. *Journal of Applied Physics*, 104(11):113904, 2008.

[12] Sam A. Hill and William K. Wootters. Entanglement of a pair of quantum bits. *Phys. Rev. Lett.*, 78:5022–5025, Jun 1997.

[13] Ryszard Horodecki, Paweł Horodecki, Michał Horodecki, and Karol Horodecki. Quantum entanglement. *Rev. Mod. Phys.*, 81:865–942, Jun 2009.

[14] Masahiro Hotta. Quantum energy teleportation in spin chain systems. *Journal of the Physical Society of Japan*, 78(3):034001, 2009.

[15] R. C. Jaklevic, John Lambe, A. H. Silver, and J. E. Mercereau. Quantum interference effects in josephson tunneling. *Phys. Rev. Lett.*, 12:159–160, Feb 1964.

[16] Daniel F. V. James, Paul G. Kwiat, William J. Munro, and Andrew G. White. Measurement of qubits. *Phys. Rev. A*, 64:052312, Oct 2001.

[17] B.D. Josephson. Possible new effects in superconductive tunnelling. *Physics Letters*, 1(7):251–253, 1962.

[18] A. Lupaşcu, E. F. C. Driessen, L. Roschier, C. J. P. M. Harmans, and J. E. Mooij. High-contrast dispersive readout of a superconducting flux qubit using a nonlinear resonator. *Phys. Rev. Lett.*, 96:127003, Mar 2006.

[19] A. Lupaşcu, C. J. P. M. Harmans, and J. E. Mooij. Quantum state detection of a superconducting flux qubit using a dc-squid in the inductive mode. *Phys. Rev. B*, 71:184506, May 2005.

[20] Eduardo Martín-Martínez, Miguel Montero, and Marco del Rey. Wavepacket detection with the unruh-dewitt model. *Phys. Rev. D*, 87:064038, Mar 2013.

[21] Eduardo Martín-Martínez, Alexander R. H. Smith, and Daniel R. Terno. Spacetime structure and vacuum entanglement. *Phys. Rev. D*, 93:044001, Feb 2016.

[22] Emma McKay, Adrian Lupaşcu, and Eduardo Martín-Martínez. Finite sizes and smooth cutoffs in superconducting circuits. *Phys. Rev. A*, 96:052325, Nov 2017.

[23] T. P. Orlando, J. E. Mooij, Lin Tian, Caspar H. van der Wal, L. S. Levitov, Seth Lloyd, and J. J. Mazo. Superconducting persistent-current qubit. *Phys. Rev. B*, 60:15398–15413, Dec 1999.

[24] Terry P. Orlando and Kevin A. Delin. *Foundations of applied superconductivity.* Addison-Wesley, 1991.

[25] B. Peropadre, D. Zueco, D. Porras, and J. J. García-Ripoll. Nonequilibrium and nonperturbative dynamics of ultrastrong coupling in open lines. *Phys. Rev. Lett.*, 111:243602, Dec 2013.

[26] Michael Edward Peskin and Daniel V. Schroeder. *An introduction to quantum field theory.* Perseus Books, 1995.

[27] Alejandro Pozas-Kerstjens and Eduardo Martín-Martínez. Harvesting correlations from the quantum vacuum. *Phys. Rev. D*, 92:064042, Sep 2015.

[28] C. Sabín, J. J. García-Ripoll, E. Solano, and J. León. Dynamics of entanglement via propagating microwave photons. *Phys. Rev. B*, 81:184501, May 2010.

[29] Jiahao Shi. Fast switchable ultrastrong coupling between superconducting artificial atoms and electromagnetic fields. Master's thesis, University of Waterloo, 2019.

[30] Petar Simidzija, Robert H. Jonsson, and Eduardo Martín-Martínez. General no-go theorem for entanglement extraction. *Phys. Rev. D*, 97:125002, Jun 2018.

[31] Petar Simidzija and Eduardo Martín-Martínez. Harvesting correlations from thermal and squeezed coherent states. *Phys. Rev. D*, 98:085007, Oct 2018.

[32] Stephen J. Summers and Reinhard Werner. Bell's inequalities and quantum field theory. i. general setting. *Journal of Mathematical Physics*, 28(10):2440–2447, 1987.

[33] Jin Wang, Herman Batelaan, Jeremy Podany, and Anthony F Starace. Entanglement evolution in the presence of decoherence. *Journal of Physics B: Atomic, Molecular and Optical Physics*, 39(21):4343–4353, oct 2006.